Optimization of Backplane Correction Studies Using 2017 Data of Compact Muon Solenoid Silicon Tracker

By

Adnan Khan

A DISSERTATION SUBMITTED IN THE PARTIAL FULFILLMENT OF THE REQUIREMENT FOR THE DEGREE OF MASTER OF PHILOSOPHY

Department of Physics
QAU, Islamabad
Pakistan,

CERTIFICATE

The undersigned hereby certify that they have read and recommend to the Department of Physics for acceptance of thesis entitled **"Optimization of Backplane Correction Studies Using 2017 Data of Compact Muon Solenoid Silicon Tracker"**, by **Adnan Khan, Roll No: 02181613015** in partial fulfillment of the requirements for the degree of **Master of Philosophy**.

Dr. Ashfaq Ahmad
Supervisor
Director
Experimental High Energy Physics
National Center for Physics
Quaid-i-Azam University,
Islamabad.

Prof. Dr. Arif Mumtaz
Chairman
Department of Physics
Quaid-i-Azam University,
Islamabad.

DEDICATION

To my Loving Mother.
I want to thank her for sharing the strength of love and affection, for her kindness and care, making my world much better and brighter and for being such a blessing to me.

ACKNOWLEDGMENTS

In the name of Allah, *"The Most Gracious and The Most Merciful".* All Praises to ALLAH for the strength and HIS blessings in completing this research thesis. I would like to express my sincere gratitude to my supervisor **Dr. Ashfaq Ahmad** (Director of EHEP at National center for physics) for his continuous support and guidance during my research work. Not only his scientific genius remarkable but his overall knowledge and understanding of things always impress me a lot. I also appreciate his patience, motivation, enthusiasm and immense knowledge. I could not imagine to having a better advisor and mentor for my M.Phil thesis. I also want to thank **Dr. Muhammad Shoaib**, **Dr. Muhammad Waqas** and **Iqra Sohail** for their constant and detailed support and help throughout this work. They looked after me when it came to guidance about the subject.

I would also like to thank **Haseeb Ahmad** for his encouraging behavior during my research.

I am thankful to my senior group fellow **Shahzad Ali** for his precious suggestions and constant support during my research. Sincere thanks go to my friends **Yaseen Ahmad, Arsalan Khan, Samiullah, Najmul Hasan, Waseem Sajjad, Abdul Qadir, Asif Ali** and others for their kindness and moral support during my study.

I want to thank my group fellows, **Shah Ahad, Ammad Muhammad, Sahar Javed, Huda Siddiqui, Ramsha Kanwal, Khushbakht Habib, Junaid and Muhammad Mubasher** for their contribution to friendly and pleasant working environment.

Last but not the least, my deepest gratitude goes to my beloved family especially my parents and to my brothers for their endless love, prayers, and encouragement and supporting me spiritually throughout my life. To those who indirectly contributed to this research, your kindness means a lot to me. Thanks a bunch!

Adnan Khan

Abstract

The silicon strip tracker is the central part of the CMS detector. The precise and accurate alignment of this complex tracker detector is a formidable task, and only achievable with a significant advancement in technologies. This thesis describes the **Backplane Correction** measurement using 2017 collision data of CMS. The CMS silicon strip tracker detector consists of four parts TIB, TID, TOB, and TEC. In this analysis, we measured the backplane correction for the TOB only. The silicon strip detectors consist of 15,148 highly sensitive modules read out by APV25 chips. The module APV25 chip can be operated in two different modes i.e peak and deconvolution modes. The alignment framework uses either track or hits taken in peak or deconvolution mode of data. This framework has introduced a shift (Δu) in the deconvolution mode. In this thesis, the measurement of shift (Δu) introduced by the alignment software has been studied. The average value of shift (Δu) in the sensor position of TOB is 1.03 ± 0.66 μm and the Lorentz angle is approximately 0.000053 ± 0.0000058.

Contents

List of Figures

List of Tables

Chapter 1

Introduction to Standard Model

The discovery of fundamental particles (which form all the matter in the universe) has a long history in the particle physics. The scientists have often made claims to determine the basic building block of matter. However, the scientists going deeper into the matter have revealed smaller and smaller particles. In the past twenty years they have achieved an exceptional progress in the elementary particles physics (theoretical as well as experimental). It is incredible to perceive that at the beginning of the 20th century, the structure and properties of the atom was unknown. The electron had only been discovered a few years earlier, and its behavior and properties were still not well understood. In that time nobody knew anything about subatomic particles, such as nuclei, protons, quarks, neutrinos, photons, gluon.

In particle physics, we study the basic building blocks of matter (elementary particles) and the interactions among them. But, which particle is marked as the elementary particle has changed with time.

Here we will provide an overview of the Standard Model of particles and the interaction of the particles with matter. Four fundamental interactions are responsible to act among these particles, the first one is the gravitational interaction between all known particles which is very small, weak interaction act between half-integer spin lepton. While the strong and electromagnetic interaction occurs between the color charge and charged particles respectively. The Standard Model of particles set up the mathematical and theoretical framework which contain the present knowledge of particles and three interactions respectively. The gravity is explained by the general theory of relativity [1].

Even today, experimental observations raised new questions. One example is the measurements of the Planck satellite and earlier experiments, that direct the existence of dark matter in the universe [2]. A theoretical explanation of the nature of this matter still requires to be found. Theories such as supersymmetry have been proposed and need to be confirmed experimentally.

In order to answer these questions, the Hadron Collider was built at CERN. The Hadron Collider is built to accelerate proton-proton as well as heavy ions beam and then collided its at interaction points. A brief introduction to the LHC and its research goals will also be given in this chapter. The CMS is installed at one point in the Hadron Collider. For the best spatial resolution of particle trajectory reconstruction, the CMS inner tracking systems are installed, having a pixel tracker at the center and enclosed by strip tracker detector.

1.1 Standard Model of Fundamental Particles

It was needed to build a model to organize a zoo of particles. New particles were given names like σ(Sigma), π(pi), Δ(delta) and so on even we were running to symbols the name of these particles. The particles were organized according to the property like mass, spin, charge and the lifetime. The new elementary particles called quarks were discovered and the whole zoo of particles was build by a combination of these quarks. This was the birth of the Standard Model.

The Standard Model gives a brief explanation of over 47 years of experimental as well as the theoretical field of HEP, by decreasing the discovering phenomena to the least number of fundamental particles as well as three basic interactions. The gravity is not put in the theoretical framework of Standard Model, the explanation of this phenomena is impossible with Standard Model.

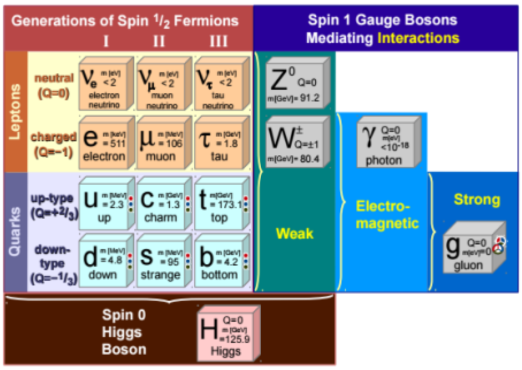

Figure 1.1: The Standard Model of particles, grouped into fermions, gauge boson, and the Higgs particle. The upper left values in each box correspond to the mass, charge, and spin, respectively.

The SM is curious to understand elementary particles, the forces and the kind of interactions between them. The Standard Model has embodied our current understanding by providing the integrated forms of forces, and the interactions through which the fundamental particles of the Standard Model interact.

1.2 Constituents of Standard Model

All the basic interaction and phenomena are embodied in the Standard Model, the outcome of theoretical as well as experiment growth both are combined from many decades. The Dirac wrote his first greatest paper in 1927 in which he combined the quantum theory of radiation with classical mechanics. The discovery of antiparticles in 1932 and the extension of relativistic phenomena were the opening of the numerous progression of the SM with its fermion achievement in 2000 with the discovery of the τ-neutrino [3].

The Standard Model consist of two type of particles that are differentiated quantum mechanically.

- **Matter Particles**
- **Quanta of Force**

1.2.1 Matter Particles

In the Standard Model the matter particles consist of fermions, which have half integers spin(1/2) and accept the Pauli exclusion principle. The fermions are further divided into two categories quarks and lepton, these two categories are further divided into three families as shown in figure 1.2. In each family, there are two type of particles, charged particles and other are neutral particles. The charged particles in lepton pair interact through weak and electromagnetic interactions and the neutral particles interact through only weak interaction (neutrino(ν)). Similarly, quarks family interacts through weak and electromagnetic interaction.

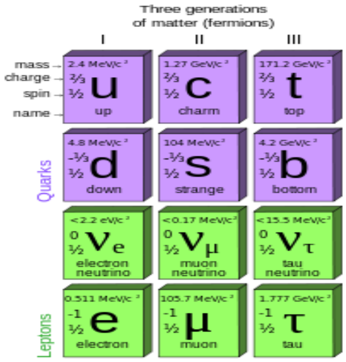

Figure 1.2: The matter particles of SM are assembled in two categories in three family.

In a contradiction to the leptons, the generation of quarks also interacts through strong interaction, which is showed by the extra color charge. The electroweak interaction distinguishes between left and right handed particles,

further each family is divided into a right-handed singlets and doublet quark and left handed lepton. Each generation only distinguish between the particles masses and they are the free parameters of Standard Model and thus only available by measurement.
The quarks contain the colors property which has define their state. The color charges keep the quarks in bound state and results from a relative massive form called Hadrons. Relativistic quantum theory gives its mathematical explanation of Dirac Equation to study the tendency towards fundamental particles. Dirac equation also incurred to rationalize the anti particle by showing their charge with negative sign but keeping mass same as that of particles.

1.2.2 Quanta of Force

All fundamental interactions are represented by the exchange of intermediate particles in the SM. Therefore, the Standard Model consists of other categories of particles known as intermediate particles, which are associated with the four interactions. These particles are bosons with integer spin. The intermediate particles of electromagnetic interaction are γ, and the mediator of strong interaction is gluon g, all quantum numbers are conserved i.e charge conjugation C, parity P, time reversal T, lepton number L, baryon number B and the flavor quantum numbers.

Table 1.1: The mediator for different interaction.

Name	**Mass** GeV/c_2	**Electric charges**	**Spin**	Interaction
γ	0	0	1	Electromagnetic
$W^{\pm}$	80.40	$\pm$	1	Weak
Z^o	91.188	0	1	Weak
gluon	0	0	1	Strong

The weak interactions are divided into neutral and charge mediator. The neutral particle is represented by Z boson, it is interacting with left and right handed particles. The other is charge particle represented by W boson, its violates P (parity) and C (charge conjugation) and interacted only with left-handed particles. These are able to change the flavor of a particle. The neutral particles is not able to change the flavor, according to the GIM mechanism the prediction of charm quark is given before its discovery [4]. Moreover the accurate estimation regarding about the Z boson, its decay at LEP to all particles except the fourth generation.

1.2.3 Higgs Particle

The Higgs particle is the last discovered particle of the Standard Model, detected in 2012. This is a phenomenal discovery and latest confirmation of the Standard Model. The mass of Higgs Boson is 125 GeV and spin zero, among other Standard Model particles with either half-integral or integral spin.

The Higgs field giving masses to other particles of the Standard Model and they will be massless and if Higgs Boson is not considered in Standard Model of particle the universe will be left in a distinct horizon. The zero mass particle could move with the speed of light. There is another particular characteristic of Higgs Boson: it is non-zero vacuum expectation valued while the rest of elementary particles of the Standard Model have zero expectation values in a vacuum. According to modern Physics, Higgs Boson is driven by Higgs Field excitations. The discovery of Higgs Boson is also acceptance of Electroweak Scale that is of the order of 100 GeV and it proves that electroweak gauge bosons are connected to Higgs Mechanism.

1.3 Four Fundamental Interaction

All fundamental particles interact with each other through the fundamental interaction known as:

- **Electromagnetic forces**

- **Weak force**
- **Strong force**
- **Gravitational force**

1.3.1 Electromagnetic Interaction

In classical mechanics the electromagnetic interaction can be explained in terms of scalar potential. But the classical mechanics explanation does not give a good result. For example the scattering of electron under the nuclear potential is a process of momentum transfer between two bodies without any evidence of mediator particle. This description of classical electromagnetism can not explain the origin of interaction.

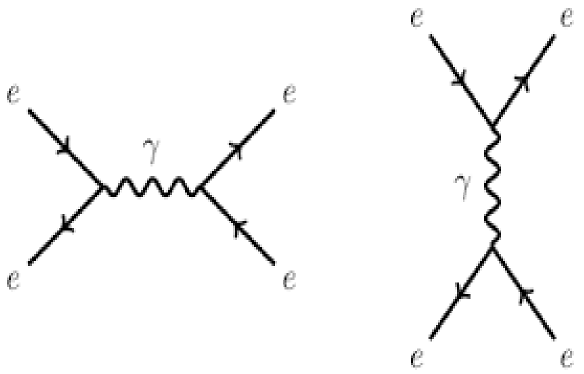

Figure 1.3: The exchanging of photon between two electrons in QED.

Modern theory (QFT) carries the explanation of every interaction. In case of electromagnetism the Quantum Electrodynamics (QED) explains the phenomena through mediators called "Virtual Photons". Figure 1.3 shows the interaction through photon. In the left diagram the electron emits photon which is absorbed by the second electron. While the second diagram shows the other way round transfer of photon which is emitted by lower and absorbed by upper electron.

1.3.2 Strong Interaction

Strong force holds several nucleons together in nucleus against the electromagnetic repulsion force between protons-protons. The strong force is charge independent. The range of the strong interaction is about 10^{-15}m (1 femtometer) and the interaction time is so small which is about 10^{-23}s. This is roughly the time taken by light to travel across a proton. In 1935, Yukawa explained this force at the nuclear level through the exchange of particles called pions [5, p.323]. However, the dimensionless coupling constant representing the strength of strong interaction is about fourteen, indicating that the strength of the electromagnetic force is about a one thousandth part (10^{-3}) of the strong interaction. Strong interaction is responsible for alpha decay in the nuclear reaction. In fact, the strong interaction also occurs at the quark level through the exchange of massless gluons carrying spin 1 and nuclear forces are expected to be residual forces arising out of the quark level interaction.

1.3.3 Weak Interaction

Unlike other interactions, weak interaction is unique in a sense that it does not form any bound system, and shows only decay of particles. For instance, weak interaction is responsible for all radioactive decays. The range of weak interaction is very small which is about 10^{-18}m, which is about 0.1 percent of the diameter of proton. The dimensionless coupling constant for the weak interaction is 10^{-13} and the interaction time is 10^{-10}s. In 1934, Fermi developed the first theory of weak interaction which is known as Fermi theory of beta decay. Later the weak interaction was thought to be manifestation exchange of certain spin one particles. Final theory of weak interaction, known as the Glashow, Weinberg and Abdus Salam theory developed in 1967. In this theory the intermediate particles of weak interaction is W^+,W^- and Z^0 [5, p.334]. They have masses, mass of W boson is 80.40 GeV and that of Z boson is 91 GeV and spin of both is one as shown in the table 1.1.

1.3.4 Gravitational Interaction

The gravitational interaction was the first interaction known to humans. This law was formulated in 1966 by Newton. The gravitational interaction is responsible for keeping heavenly bodies like moons, planets, and stars in their orbits. It is always attractive and its range is infinite. In order to compare the relative strength of different interaction, we define a dimensionless coupling [5, p.322] constant as

$$g_m = G_N \frac{m^2}{\bar{h}c} \tag{1.1}$$

where g_m is dimensionless coupling constant, G_N is gravitational constant which is equal to $6.66 \times 10^{-11}\ Nm^2/kg^2$, m is the mass of objects between which gravitational interaction is operating, $\bar{h} = h/2\pi$, h is the Planck's constant and c is the speed of light. The dimensionless coupling constant between nucleons can be calculated by taking m $= 1.67 \times 10^{-27}\ kg$

$$g_m = 2\pi \times 6.66 \times 10^{-11} \times (1.67 \times 10^{-27})^2/6.626 \times 10^{-34} \times 3 \times 10^8 \tag{1.2}$$

$$g_m = 6 \times 10^{-39}$$

This interaction is universal, i.e every massive particle experience gravitational force. The carrier of gravitational interaction is conjectured to be a graviton. The mass and spin of the graviton is zero and two respectively, thus it travels with velocity which is equal to that of light. This interaction is extremely small for elementary particles and hence is usually neglected.

1.4 Particle Interaction with Matter

When a particle interacts with matter a number of particles are formed, the different type of experiments are designed to detect these particles depending upon their type. They contains stable and unstable particles. The stable particles consist of photon, electron, proton and the massless and undetectable neutrinos. The unstable particles decay after moving a $\gamma \upsilon \tau$ distance, where

τ is the decay constant, v is the velocity and

$$\gamma = \frac{1}{\sqrt{1 - \frac{v^2}{c^2}}} \tag{1.3}$$

The unstable particles are consisting of long-lived and short-lived particle. If the particles decay within 10^{-10} second they are grouped into short-lived particles while particles decay after this time are known as "relatively long lived particles". These particles consist of charged π^+ and π^- and charged K^+ and K^-. The relatively long-lived and stable particles are the product of the particles which is detected in the particle collision experiments.

1.4.1 Energy Lose of Heavy Charge Particles

When a charged particles are moving with the speed of light "c" and pass through a matter get ionized under the electromagnetic interaction and lose their energy. The Bethe-Bloch [6] equation below explaining these energy loss.

$$\frac{\mathrm{d}E}{\mathrm{d}x} \approx \frac{-4\pi^2 c^2 \alpha^2 \hbar^2 n Z}{m_e v^2}[ln(\frac{2\beta^2\gamma^2c^2m^e}{I_e}) - \beta^2] \tag{1.4}$$

Consider a particle moving with the v=c, atomic number "Z" and "n" is number density. Here I_e is the mean value of effective ionization potential for all atomic electrons which is dependent on the material being used and it is of the order of $I_e \approx$ 10Z eV. For particular medium, this ionization potential depends on velocity so energy loss by Bethe-Bloch equation will be greater for low velocity particles. But in modern particle physics, relativistic particles are of the major interest, then the Bethe-Bloch energy lose which varies logarithmically as shown in figure 1.4 on the $(\beta\gamma)^2$, undergoes through small variations where

$$\gamma\beta = \frac{\frac{v}{c}}{\sqrt{1 - \frac{v^2}{c^2}}} \tag{1.5}$$

This rate of energy loss depends on the density of the material "ρ" which can be seen from the atomic number density $n = \frac{\rho}{Am_u}$ here A = atomic mass number, m_u = unified atomic mass unit and now equation (1.4) can be written as

$$\frac{1}{\rho}\frac{\mathrm{d}E}{\mathrm{d}x} \approx \frac{-4\pi^2c^2\alpha^2\hbar^2Z}{m_e v^2 A m_u}[ln(\frac{2\beta^2\gamma^2c^2m^e}{I_e}) - \beta^2] \tag{1.6}$$

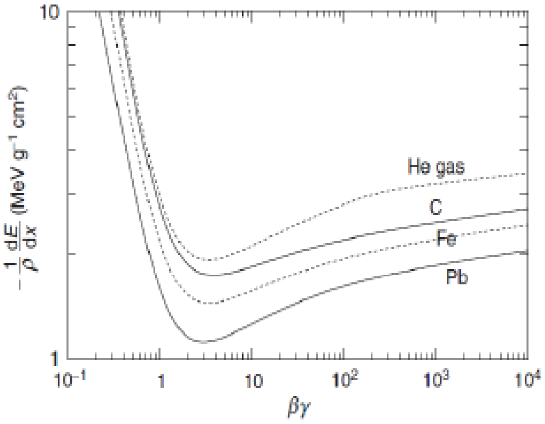

Figure 1.4: The ionization energy loss curves for a singly charged particle traversing gaseous helium, carbon, iron, and lead [2].

Equation (1.6) shows the proportionality between dE/dx and Z/A. Depending on the type of particle. Muon is least ionizing particle, so it penetrates through small distances in the material, even in dense iron material muon move with 100 GeV, energy loses a maximum of 13 MeV cm^{-1}. Due to this property muon moves through the longer distance in the detector and leaves a long track in the detector medium. All other charged particles have different kinds of interactions in addition to ionization energy loss.

1.4.2 Energy Lose of Electron and Photon

If the energy of an electron is low, it loses energy through ionization process. When the particle energy is less than a E_c range the ionization is carrying out by bremsstrahlung. While an electron is moving in electrostatics field they emit photon. The critical energy is described in the form of nuclear charge as $E_c \approx \frac{800}{Z}\ MeV$.

In particle physics the most process is found in various range and the range of an electron is greater than critical energy range, hence the interaction with the matter occur through bremsstrahlung. The bremsstrahlung energy loss is inversely proportional to the mass of the charged particle. That's why the energy loss by muon is suppressed by (me/m_u). Therefore the main process of energy loss for an electron are bremsstrahlung.

- In photoelectric effect, the low energy interaction occurs with the photon, while the atomic electron ingests the photon.
- At higher energy, the order of $E \sim MeV$, Compton scattering process dominates.
- When energy increases from E > 10 MeV, process of pair production e^+e^- is dominant.

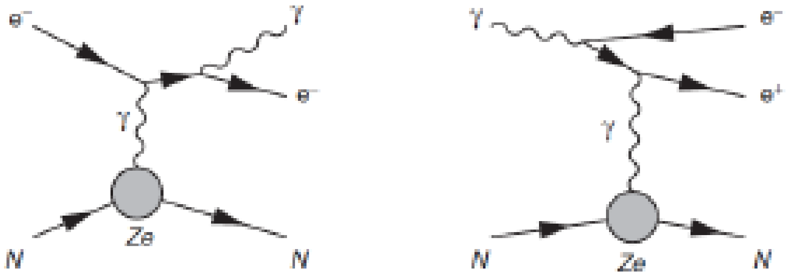

Figure 1.5: In the pair production of electron and positron the energy lose by bremsstrahlung radiation.

The electromagnetic interactions for high energy photons and electrons are indicated by radiation length X_o. The radiation length explains the mean distance for which the energy loss through bremsstrahlung occurs of the order of $\frac{1}{e}$.

$$X_o = \frac{1}{4\alpha n Z^2 r_e^2 ln(287 = Z^{\frac{1}{2}})} \tag{1.7}$$

here Z = atomic number of material, n= nuclear number density and r_e = classical radius of electron which is expressed as:

$$r_e = \frac{e^2}{4m_e c^2 \pi \epsilon_o} = 2.8 \times 10^{-15} m \tag{1.8}$$

The inverse relation between Z and the X_o interprets that, for the materials with higher Z values, X_o will be shorter. For example, lead and iron have radiation lengths of $X_o(Pb) = 0 : 56\ cm$ and $X_o(Fe) = 1 : 76\ cm$ respectively.

1.5 Accelerators in Particle Physics

Most of the discovery have come in particle physics from the experiment. The experimental set up have two types:

- Colliding Beam Experiment: In colliding beam Experiments, two traversing particles beam are colliding.
- Fixed Target Experiment: In fixed target experiments, a single beam is colliding with a fixed target.

For the production of heavy particles, like W^+,W^-, Z and Higgs bosons, high energies are required. The energy production from the sum of the masses of two particles is lesser than the energy in the center of mass coordinate. The COM is the square root of the Lorentz Invariant quantity R, with the natural units c = 1, $\hbar$ = 1 it is given by:

$$R = (\sum_i^2 U_i)^2 - (\sum_i^2 P_i)^2 \tag{1.9}$$

In fixed-target experiment, the momentum conservation shows that the final state particles are always generated with the significant K.E and a large amount of initial energy is definitely wasted. For example, if a proton with E = 7 TeV , collides with a proton at rest, it will give a center of mass energy of only 115 GeV.

$$R = (E + mp)^2 - p^2 = 2m^2p + 2mpE \approx 2mpE \tag{1.10}$$

The importance of colliding beam experiment is that they can achieve much higher COM since the collision occurs in the center of mass frame. For example, at LHC two beams of 6.5 TeV protons are collided, giving a center of mass energy of 13 TeV. Due to these advantages, almost all high energy particle experiments are based on the large particle collider.

Only the charged stable particles can be accelerated to the high energy, therefore possible types of accelerators are installed in hadron collider such as proton-proton, proton anti-proton, electron-positron, and electron–proton collider. The two most important terms of an accelerator are its instantaneous luminosity L_{ins} and COM, L_{ins} measures the event rates and COM determines types of the particles that can be discovered. For a given collision, the number of interactions is:

$$N = \sigma \int L(t)dt \tag{1.11}$$

Cross section σ gives the probability of interaction, depends on the fundamental process elaborated in the Feynman diagrams.

The particles in an accelerator are assembling into bunches which are brought into collision at collision point. At these collision point detectors are installed. At LHC, the bunches spacing is 25ns and the collision frequency is 40 MHz. The L_{ins} can be represented is:

$$L = f\frac{n_1 n_2}{4\pi\sigma_x\sigma_y} \tag{1.12}$$

n_1 and n_2 are the number of particles, σ_x and σ_y are the root mean square horizontal and vertical beam sizes.

The correct properties of the colliding beam experiment, like the transverse properties are not known correctly and therefore it is impossible to absolutely determine the L_{ins}. Therefore the cross section measurement is executed with reference to the process where cross section is already known. For the measurement of cross section we need the number of events N, and number of the observed events for reference process N_{ref}, so that the measured cross section is

$$\sigma = \sigma_{ref}\frac{N}{N_{ref}} \tag{1.13}$$

1.5.1 The Hadron Collider

The Hadron Collider explained the physics phenomena at the 13 TeV range energy to give the confirmation of the Standard Model at high energy. The discoveries of extra dimension, super symmetry and physics beyond the Standard Model is also the goals of Hadron Collider. The phenomena of the Hadron Collider also assimilate heavy ion collision to produce a broad description of QCD, that follows the intense circumstances of temperature, density and parton momentum fraction.

The circumference of Hadron Collider is 27 km. The constructed luminosity is L = $10^{34} cm^{-2} s^{-1}$ and COM energy for proton-proton collision is 13 TeV. The 1332 Superconducting Dipole Magnets installed to produce the Magnetic Field 8.4 Tesla to keep the 13 TeV proton beams at the 27 km circumference circle [7]. To provide the secure process of the device and for the stability of magnetic system the preservation systems are used. In the first commissioning a technical incident occur in the Hadron Collider in September 2008, LHC was set to operate at a COM energy of 7 TeV, additionally to upgrade of the QPS for the Dipole Magnets has installed, which is foreseen to occur during a major shutdown in 2013 [8]. Initially the protons beams are accelerated in the 26 GeV PS booster, then its accelerated to 450 GeV in the SPS booster, after this they are injected to the Hadron Collider.

Figure 1.6 shows the four main detectors, that are installed at four different point of the Hadron Collider. The ALICE is heavy ion collision detector [9], LHC-b for the study of CP-violation in decay of b-meson [10]. The two general purposes detector are ATLAS and CMS [11]. These two detectors measure the proton-proton interaction and help to confirm the luminosity of Hadron Collider as well as to study the physics phenomena produce at high energy. The LHC-f4 consists of two main detectors, 140 m away from both side of the ATLAS experiment [12]. The TOTEM5 detector consists of many modules at a distance 220 m away from the CMS detector. Both the general purposes detectors ATLAS and CMS are build for the confirmation of Standard Model and physics beyond the Standard Model. The detail explanation of CMS detector are in chapter 2.

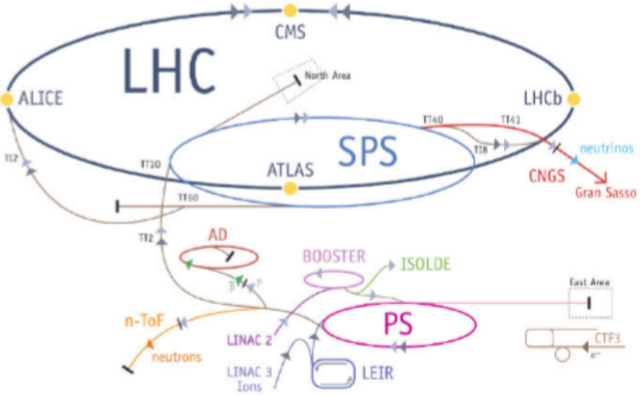

Figure 1.6: Different Detector layout in Hadron Collider.

1.5.2 Process Before the LHC Ring

Before the collision of particles in the main LHC synchrotron, they have to be pre-accelerated by various smaller accelerators as shown in figure 1.6, because of the particular design of the LHC magnets and cavities. The hydrogen atoms are stripped of their electron and are passed by the linear accelerator LINAC-2 into the Proton Synchrotron (PS) Booster. At this stage, the energy of proton is comparatively low 50 MeV. The PS Booster accelerates the protons up to 1.4 GeV, gain 91.6 % velocity of light before feeding them into the Proton Synchrotron (PS), where they are accelerated up to 25 GeV, 99.9 % of the velocity of light. The package of proton now channel to the Super Proton Synchrotron (SPS), design particularly to take the protons at this much high energy and increase it to 450 GeV. After that, the protons are launched into the LHC ring 27 km in circumference. Both clockwise and anticlockwise injection is done in order to obtain two beams. In the Large Hadron Collider (LHC) the proton beams accelerate up to 6.5 TeV, including other miscellaneous experiments placed at CERN [13].

Chapter 2

The CMS Experiment

2.1 Introduction

The CMS detector is designed for the general phenomena of physics, to examine a different form of proton-proton interaction at 13 TeV. The CMS enclosed an enormous magnet solenoid. This magnet solenoid made in the form of a cylindrical shape of powerful superconducting wire that generated an Magnetic Field of 3.8 Tesla, the Magnetic Field of this solenoid is 10^4 times greater than from the Magnetic Field of the earth. The outside Magnetic Field of the solenoid is enclosed by a steel return yoke the weight of this return yoke is 12,500 tonnes. A rare quality of the CMS is that it made and built underground like the other big detectors of the Hadron Collider. The internal sub-detectors parts as shown in figure 2.1. Which are arranged to estimate the energy and momentum of particles like electrons, muons, and other particles generated from the collision point. The pixel and SST are the innermost part of the CMS. It is enclosed by a scintillating crystal ECAL, which is itself enclosed by HCAL. The tracker and ECAL and HCAL are sufficiently small to put inside the solenoid which generates a powerful Magnetic Field of 3.8 Tesla. Outer sub-detector part of CMS is the large muon station, enclosed by the return yoke of the magnet.

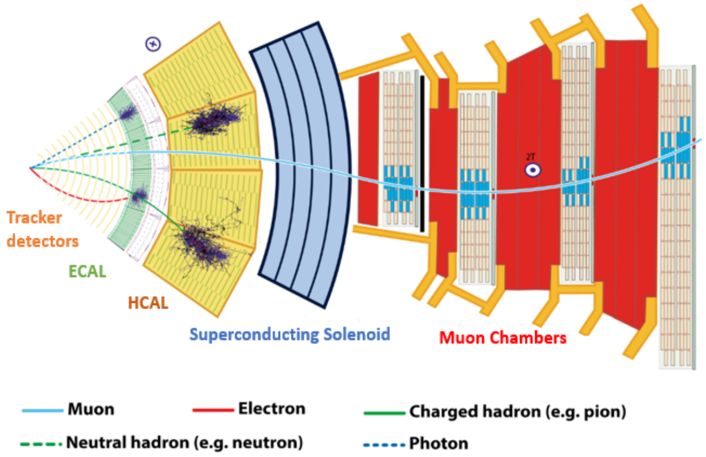

Figure 2.1: Internal layout of all sub detector of Compact Muon Solenoid [14].

The scheme of the Hadron Collider is not the only challenge, they also need high-quality technical demand for analysis of data which is coming from the interaction point after every 25 ns. At the design luminosity, one event significantly is composed of twenty-two inelastic collisions. As a result, a hundred charged particles coming out from the interaction point. The pile-up process used to check a detectors which are high granularity and time resolution. For the millions of processing channels we need a high granularity.
The high flux which is coming from the collision point damages the detector and read out micro-electronics. The detectors and micro chip must be radiation hard. The Hadron Collider explain the following phenomena as shown in the points [14].

- Di-muon, di-electron and di-photon mass resolution of about 1% at 100 GeV.

- To determine the charge and momentum of Muon, where the momentum "P>1 TeV".

- To specify the high reconstruction efficiencies and momentum in the tracker, to provide triggering and tagging of particles from secondary vertices, such is tau leptons and b-jets.

- Good resolution of E_{miss} (MET) and di-jet.

2.2 CMS Co-Ordinate System

There are two types of coordinate system.

- Global Coordinate System.
- Local Coordinate System.

2.2.1 Global Coordinate System

The global coordinate decided to explain the phenomena estimated in the various part of the detector. The z-axis along the beam of the proton, while both x- and y-axes are perpendicular to the z-axis. They makes a plane perpendicular to the z-axis. The y-axis perpendicular to the interaction point and x-axis towards the interaction point. In the xy-plane, the "ϕ" is measured with respect to the x-axis. The "θ" is measured in terms of pseudo-rapidity "η" which is given by

$$\eta = -ln(tan(\frac{\theta}{2})) \tag{2.1}$$

The distance b/w two particles is estimated by the following equation:

$$\Delta R = \sqrt{(\Delta\eta)^2 + (\Delta\theta)^2} \tag{2.2}$$

2.2.2 Local Coordinate System

While the local coordinate is decided for each module, the center of module plane is the origin of the coordinate. As shown in the left part of figure 2.2, the u-axis is pointing along the azimuthal direction in the global coordinate, the v-axis perpendicular to the u-axis, denoting and showing away from the readout microelectronics, and the w-axis is the upward direction from the module plane.

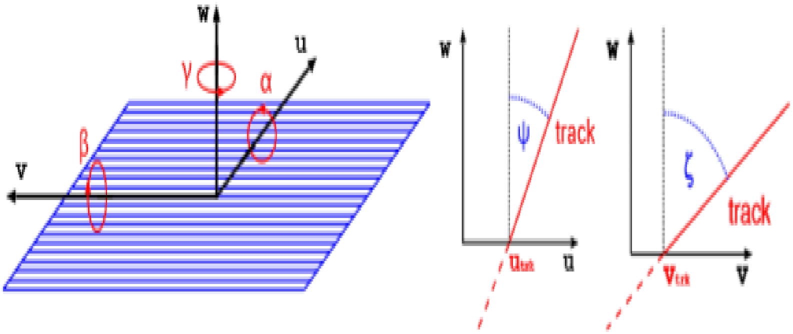

Figure 2.2: The local coordinate of module showing, the axes of local coordinate on the module plane, u, v, and w, and local rotations α, β, γ (left side), with the local track angles ψ and ζ (right side).

The center point of the module is the origin of w-axis. For the tracker detector, u are decided perpendicular to the Magnetic Field, i.e. in the global $r\phi$ plane in the barrel region and in the radial area in the end caps region. The v-coordinate is making a right angle with u-coordinate in the module plane, i.e. adjusted the global Z in the barrel and at a small angle to the global $r\phi$ direction in the end caps. The angles α, β, and γ shows right-handed rotations around the u-,v-, and w-axes. As shown in the right part of figure 2.2, the local track angle $\psi(\zeta)$ with respect to the module orthogonality is defined in the v-w planes.

2.3 The CMS Tracker Detector

The SST is the innermost part of CMS which consists of pixel and silicon micro-strip tracker.

2.3.1 Silicon Pixel Detector

After the interaction of protons at the collision point of CMS, any particle emitting from the interaction point and traveling outwards will first pass through the pixel detector.

The pixel part contains three silicon layers and two discs in the barrel and forward region receptively. The 53 cm is extended the barrel region and the three layers are situated at 4.4 cm, 7.3 cm and 10.2 cm from the beam line to permit the best reconstruction of primary and secondary vertices's. The η-range of first layer and the second disc are 2.5 respectively, balancing the approval of the barrel tracker region. Moreover, the absolute measurement of tracking region significant for the physics. The pixel is installed in the innermost part of CMS, according to the running situation.

The pixel part is composed of 1440 modules with a total active area of 1 m^2. At Hadron Collider the luminosity is 10^{34} $cm^{-2}s^{-1}$ and hit rate is 1 MHz/mm^2 at a range or radius of 4 cm. To provide 1% occupancy, the radius of the pixel part is necessary which is less than 10cm. For the achievement of expected impact parameter resolution, the area of a pixel was decided to be 100 x 150 μm^2 in the rϕ plane, as a result the holding is 10^{-4} per pixel and Hadron Collider bunch crossing. The drift of electron in the pixel part is orthogonal to the Magnetic Field. In case of a Magnetic Field the appearing of Lorentz drifts the incoming charge signal is spreading more than 1 pixel. For the insertion of charge using the APV25 read-out electronic channel to provide a spatial resolution of 15 to 20 μm [14], the performance of this could be increased by using a template fits for the hit reconstruction [15]. For the sharing of charge in the end-caps, the forward region of detectors is tilted by 20^o in a turbine-like shape.

Due to the large radiation absorption in the inner layer of the pixel part, it assemble during Hadron Collider operation i.e the working and read out channel of the pixel part have been constructed in order to provide the easy approach for the important substitution. It is important to fit the pixel modules in cylindrical rod as shown in figure 2.3. Its is separated vertically for installation in the presence of beam. Approximately 1440 modules are installed in the pixel region, read out by 65 million channels. Each pixel generated around about 50 μW power, the total power overheat the detector. Therefore the pixels part is adjusted in cool tunnels which is cool down the pixel part in a running temperature of -10^{o}C using the composite material C_6F_{14}. In 2010 the luminosity of Hadron Collider was lower and the pixel is running on large temperatures [16].

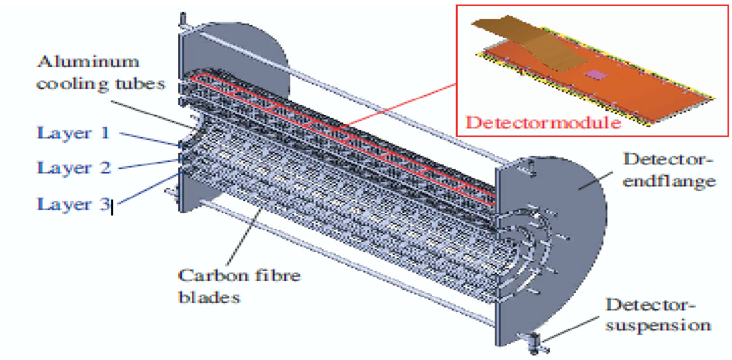

Figure 2.3: The half cylindrical support structure of pixel detector and module.

2.3.2 Silicon Strip Tracker Detector

When the distance increased from the beam line the flux of particles decreases and provided the use of a strip tracker detector. For the in-between radius (20 cm < r < 55 cm) the SST inner barrel and inner discs are installed, in the forward region the thickness of the SST sensors are 320 μm, with the module parallel to the beam axis in both region. The tracker inner barrel consists of 4 layers, these four layers are subdivided into four sub-part (±z, up/down) for the approach and integration. In first and second layer the Pitch varies from 80 μm and third and four layer the Pitch varies from 120 μm. The tracker inner barrel providing a single point resolution of 23 μm and 35 μm. The tracker inner discs region are assembled in three discs placed between ±70 cm and ±100 cm. The TID Pitch varies from 100 μm to 141 μm. To combine both tracker inner barrels and tracker inner discs cover a range in pseudo-rapidity η up to 2.500 [14, p.65].
The outer parts of the tracker detector consist of a tracker outer barrel and

tracker end caps, the thickness of TOB and TEC sensor is 500 μm. The tracker outer barrel is arranged in six layers of radius 116 cm. In the first four layers the strip Pitch varies is 183 μm and for five and six layers strip Pitch varies are 122 μm. The single point resolution of the tracker outer barrel is 53 μm and 35 μm, respectively. The tracker inner barrel and tracker inner discs module is assembled with one silicon sensor, in the outer barrel the modules are assembled with two sensors [14, p.62].
In the outer barrel region, six to twelve modules are assembled in the rods. The total dimension of the beam axis is covered with two rods. The tracker outer barrel consists of a 2.8 m long cylindrical support structure which is made by four similar discs connected by three inner and three outer cylinders, carrying 688 rods. The rods are installed in such a way that the projection of the rods laying in the $r\pi$-plane to measure two back-to-back hits [14, p.67]. The plain cylinder working has been thoroughly calculated through photogrammetry, theodolites, and 3D frame measurement systems [14, p.68]. The region of Strip tracker is spread to both face of the tracker end caps, they covered the range between 124 cm < |z| < 282 cm and 22.5 cm< r <113.5 cm. The end caps region consists into nine discs of silicon, each contains up to 7 rings of silicon. In the outer three rings are assembled with thick sensor of 500 μm, while the innermost four rings are arranged with 320 μm thin sensor. The mean pitch of the ring like strips varies between 97 μm and 184 μm, depending on the shape and type of module. Each module of TEC equipped with two sensors. Figure 2.4 shows the tracker different geometries. The local coordinate system of the module in which one perpendicular (w) to the module, the barrel region module laying in the global rϕ plane while end caps module laying in the ϕ plane. The other coordinate(u,v) is parallel to the module, z in

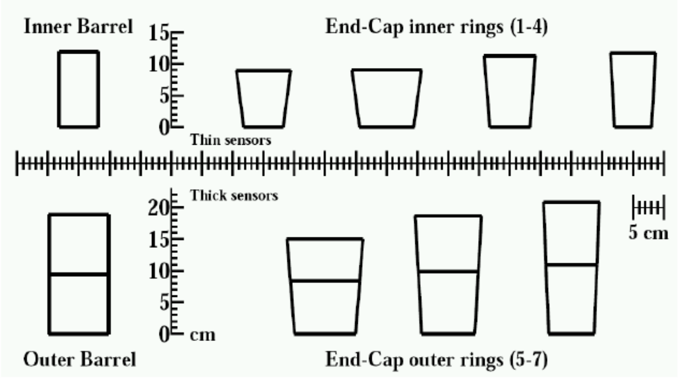

Figure 2.4: Silicon strips tracker different module, some module is equipped with one sensor and some are arranged with two sensors.

the barrel and r in the end caps region. The layers 1,2 of the inner-outer barrel and rings 1,2 of the inner dices as well as 1,2 and 5 rings of the end caps are assembled with a 2 sensor which is fitted back-to-back to the normal modules with a stereo angle of 100 mrad(see in figure 2.5).

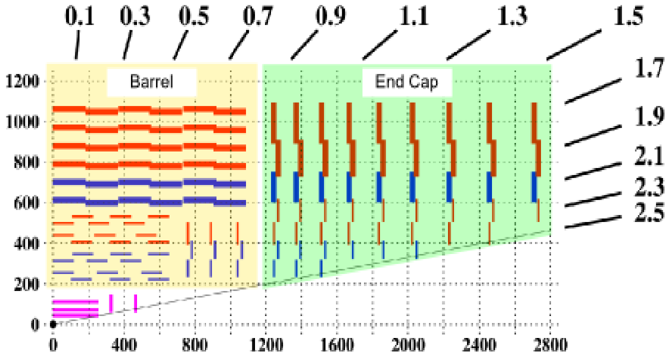

Figure 2.5: The tracker layers are arranged with one side (blue) and two side sensors (red).

The estimated single point resolution along the z-axis in the barrel region is 230 μm and 530 μm respectively, the radial coordinate calculate in the end caps which is varies with the strips Pitch.

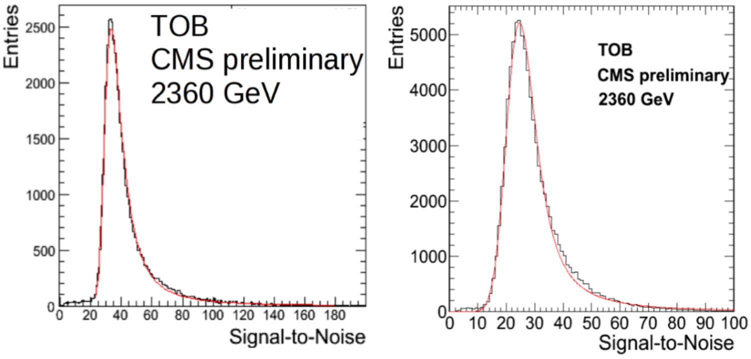

Figure 2.6: Signal to noise distribution of tracker outer barrel for two different mode one is the peak mode (left) and other is deco deconvolution mode (right) [18].

The CMS silicon strip tracker contained 15,148 micro-strip modules. Precise information about each module is vital for the physics phenomena. To restrict the installation accuracy for the module position track-based alignment is necessary and to implemented positional adjustment in the reconstructed of the trajectory, it improve the precision of the track constant parameter concluded through the trajectory fit.

The single-sided operation of the sensors, the sensor is not completely smooth but show an important bow, especially for the thick sensors [14]. The bow is less than 100 μm.

Two different readout mode can be used to take the data from the strip module, so known as peak and deconvolution mode [17]. The charge is collected in peak mode is deduced by the height of the signal. These peak signals has arrived after every 50 ns. In case of deco mode, the output charge is collected from each strip in form of a weighted sum of three sequentially pipeline cells explained in chapter 3, this process decreases the readout time of the 25 ns between two consecutive bunch crossings in the Hadron Collider [18]. The signal in deco mode is reduced about ten percent while the noise is slightly higher in deco mode. To see the distribution of the signal to noise ratio in figure 2.6 for hits in the outer barrel. To compare peak and deco mode we apply a similar cut for the S/N ratio of tracks taken in deco mode compared to the track taken in peak mode, an S/N ratio cut of 18 in peak mode has to be lowered to 12 in deco mode.

2.4 Calorimetry

There are two types of calorimetry: Electromagnetic and Hadronic.

2.4.1 Electromagnetic Calorimeter

Additionally the accurate estimation of the trajectory report about a particle, its energy measurement plays a substantial role in particle description and reconstruction. For that reason, the CMS has an electromagnetic calorimeter (ECAL), that encloses the TIB, TOB while at the end cap of ECAL there is an extra pre-shower system installed for π^o refusal. The purpose of the ECAL is to measure the energy of electrons and photons. The HCAL enclosed the barrel and end caps region of ECAL, covering the η-range in the barrel is $|\eta| < 3.00$. In the barrel region it is complemented by a tail-catcher, the combined thickness in terms of interaction length is $10 - 15\lambda_I$. For the estimation of MET to make the coverage as hermetic as possible. In the forward region there is an iron and quartz-fiber CAL covering the η-rang up to $|\eta| < 5$. In the forward region an extra detectors were installed, which are CASTOR, ZDC and TOTEM detectors outside the CMS.

The ECAL are made by 61,200.00 $PbWO_4$ crystals in the barrel region ($|\eta| < 1.47900$) and in each end caps region are 7,324 crystals up to $|\eta| < 3$ range. The important properties of $PbWO_4$ crystals are they have a short radiation length ($X_o = 0.89\ cm$) and 2.2 cm Moliere radius, to make the design of ECAL treaty inside the solenoid. The area of the front face of the crystal is $\approx 22{\times}22\ mm^2$ and its width is 230 mm, which agree to 25.8 X_o. They are put in an order for $\eta\phi$ grid while in the end caps regions an xy grid with crystals of 24.7 X_o have been chosen. After every 25 ns 80% of the radiation is released. It sample is digitalized and amplified, the noise is about 40

MeV/channel. The measurement of energy is:

$$\left(\frac{\sigma}{E}\right)^2 = \left(\frac{S}{\sqrt{E}}\right)^2 + \left(\frac{N}{E}\right)^2 + C^2 \tag{2.3}$$

the above equation "S" shows hypothetical parameter, which is about 2.800% in beam experiment, the noise of module "N" is 0.12 GeV and C is a constant which is 0.3% (see figure 2.7). The dependency of energy leads to a determination $\sigma(E)$ of less than 0.5% for E = 100 GeV.

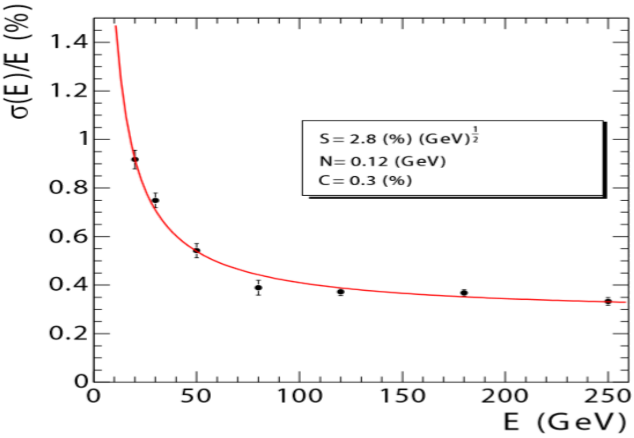

Figure 2.7: The energy resolution measured for ECAL module in beam experiment as a function of the electron energy [14].

2.4.2 Hadronic Calorimeter

The HCAL is important to measure the MET, which is significant for many phenomena beyond the Standard Model. The HCAL consists of four-part; the hadronic barrel, end caps, outer barrel and the forward region to give a coverage of $|\eta| < 5.00$. The HCAL outer barrel region is put inside the return yoke of solenoid while the hadronic forward region covered the region very close to the beam line. The HCAL forward region made outside of the return yoke and it working is an absorber material because it has non-magnetic and short radiation length. To measured the energy of strongly interacting particles the plastic scintillator tiles are read out to using a fixed wavelength-shifting fiber. The granularity of three hadronic part has been aligned in such a way that the jet energy resolution depends (as a function) on missing transverse energy as shown in figure 2.8. The jet energy resolution is a function of missing transverse energy E_T as shown in figure 2.7 for the different part in $|\eta|$.

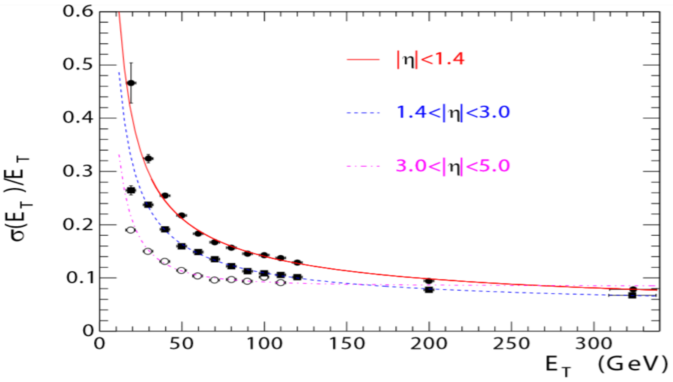

Figure 2.8: The missing transverse energy of jet as function of the simulated jet E_{miss} (MET) for the HB, end cap HE and forward HF region [14].

2.5 Muon Stations

The outermost part of compact muon solenoid is the muon station. Figure 2.9 shows the sketch of the barrel and end cap area of muon station. The muon station has a large surface area and several misty radiations they would be damage the technology. Four layers of drift tube chamber (DTC) are installed in the barrel region to cover the range of pseudo-rapidity ($|\eta| < 1.2$), separated from each other by return yoke layer. To measure the muon coordinate the first three stations are used in the rϕ-plane and the fourth one gives a measurement in the z-direction along beam direction. The rate of neutron background is much higher so in the forward region cathode strip chamber is install, as they have high resistance, good segmentation, and speed up response to the radiation. At the end cap again there are four stations of cathode strip chamber is install separated by yoke layers. The CSCs are orthogonal to the beam axis and run spirally outwards to provide a measurement in the $r\phi$-plane. The strip is installed perpendicular to the anode wires and thus give a measurement of $|\eta|$ and the beam-crossing time of the muon. In combined form both the stations to covered the $|\eta| < 2.4$.

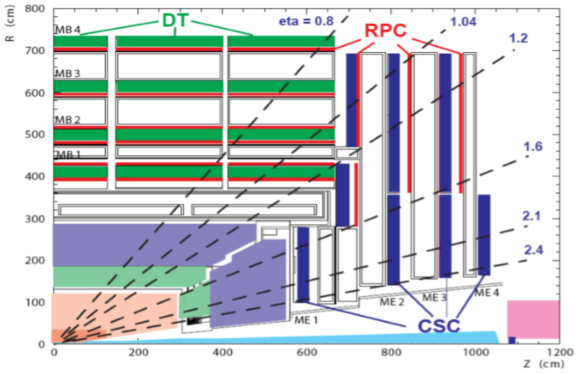

Figure 2.9: Sketch of four muon stations (MB1-MB4) are installed BR. In the end-caps ME1-ME4 a coverage of $|\eta| = 2.400$ [15].

The weakly interacting particle (muon) passing through all detector without losing much energy, before they reached the first muon chamber they are subjected by multiple scattering in various part of detectors the transverse momentum resolution of muon reconstruction using the information on system only is about 9 % for small values of $|\eta|$ and momentum up to a muon P_t of 200 GeV. The information adding from the tracking part to the global muon fit, the low momentum region can be improved as shown in figure 2.10

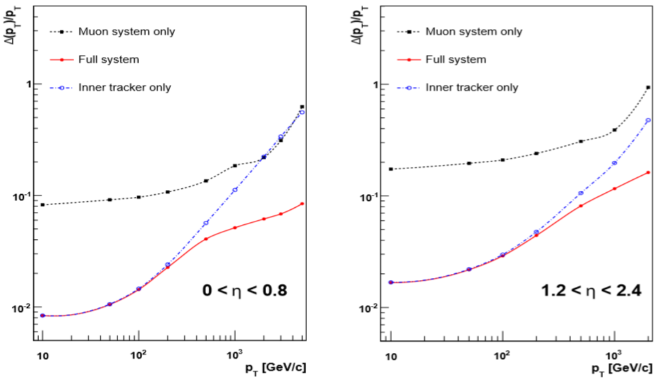

Figure 2.10: Muon reconstruction efficiency measure from muon station and from the combine detector including tracker [14].

The momentum resolution with $P_t > 1$ TeV for muon using the mixed information can be better than from complementary information of the two stations, even though the separate measurement from the muon and tracker detector are of the same magnitude.

Both the drift tube and the cathode strip chamber can each trigger for the P_t of muon with the best efficiency estimation and high background rejection. The resistive plate chamber are installed additionally in both region barrel and end caps, which give highly and fast segmented trigger with a P_t threshold over the rapidity range of $|\eta| < 1.600$ of the muon station. The RPC was added take into account the uncertainty of the background rates and to measure beam crossing time at the hadron collider design luminosity. Each layer is built to give a four-vector, with a ϕ precision better than 100.00 μm in position and 1.00 mrad in direction.

Chapter 3

Background of the Backplane Correction

3.1 Silicon Strip Detector

The silicon strip detector consists of 15 $\times 10^3$ highly over sensitive modules. The total number of strips is 10×10^6 read out by 8×10^4 microprocessor chips. Typically module shown in figure 3.1 consists of three components: the sensors, the mechanical support frame and the readout processor electronic channel.

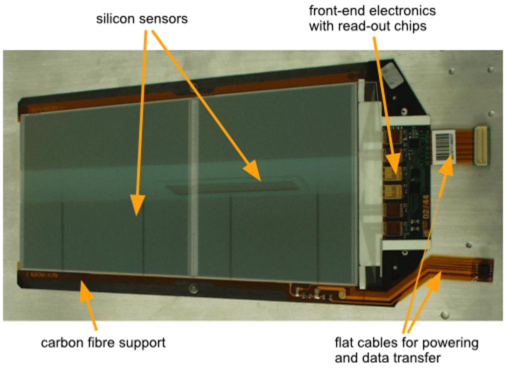

Figure 3.1: CMS silicon strip tracker (SST) detector module.

3.1.1 Working of Silicon Sensor

The working of a silicon strip sensor is used to measure the track of ionizing particles. When charge particle pass through matter they interact electromagnetically with its electron and nucleus, during their interaction they losses some of the K.E, which is measured in the form of signals.
A single particle traversing through the material, the amount of charge creation is very minute compared with the intrinsic charge carrier. The average energy losses $(dE/dx)_{avg}$ by the minimum number of ionizing particles (MIP) in silicon bulk are 388.00 eV/μm [19]. While the average energy for electron and hole pair in silicon are $E_{pair} = 3.63$ eV. The number of electron-hole pairs created by a minimum ionizing particle (MIP) in thickness (d_{Sensor} =500 μm) becomes:

$$\frac{(\frac{dE}{dx})_{mean} \times d_{Sensor}}{E_{pair}} = \frac{(388) \times 500}{3.63} \approx 5.344 \times 10^4 e^- h^+ pair \tag{3.1}$$

At temperature equal to 300 K for silicon, number of charge carrier is $n_i = 1.45 \times 10^{10}$. For silicon sensor with the similar thickness of 500 μm and an area of $A_{Sensor} = 1\ cm^2$ is:

$$n_i.d_{sensor}.A_{Sensor} \approx 1.45 \times 10^{10} \times 500 \times 1 \times 10^{-4} \approx 7.2 \times 10^8 \tag{3.2}$$

The charge generated by a minimum ionizing particle (MIP) would be four times smaller than in magnitude from the intrinsic charge generation by 1 cm^2 of silicon sensor. Hence it is significant to reduce the number of intrinsic charges. But another approach is that to operate the sensor at very low temperature, simply a much more effective approach is the use of reverse bias p-n junction.
The main component of the silicon strips sensor is the depletion region of a p-n junction. Figure 3.2 shows the working principle of a sensor, where it is operated in reverse bias p-n junction. The p-n junction is quite asymmetric while making the depletion region from the full depth of the silicon material. Accordingly, the silicon bulk is formed from the pre-doped substrate and the p-n junction is made by a heavy doped substrate. To get the complete depth

of the silicon bulk, it is significant to completely deplete it by a huge reverse bias voltage.

If an ionizing particle (MIP) passes through the depleted area, it produces electron and hole. In the presence of electric field (E) inside the bulk, the electron-hole pairs start to drift towards the electrodes and produce induce current which can be measured.

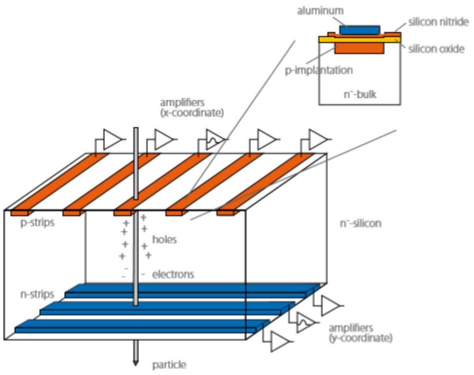

Figure 3.2: CMS silicon strip sensor layout.

The deposition of energy in thin layers of silicon are appreciably non-deterministic and following the Landau distribution, the statistical fluctuations are quite asymmetric as shown in figure 3.3. This was first expressed in [20], with a more detailed explanation and corrections to the distribution in [21].

In the foregoing calculation, the average number of electron and hole are 32.00 although due to the Landau like the behavior of the energy deposition, possible number of electron and hole are:

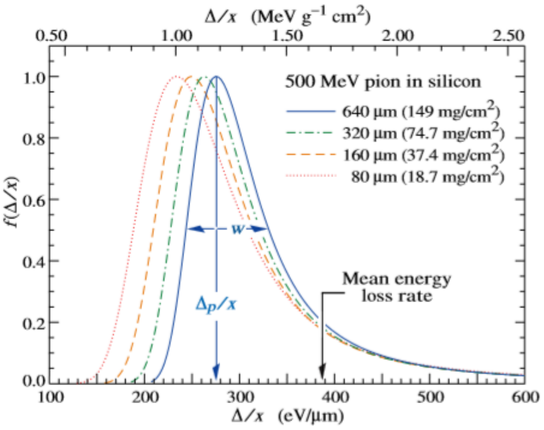

Figure 3.3: Landu distribution[19].

with $(dE/dx)_{MPV} = 276 eV/\mu$m.

$$\frac{(\frac{dE}{dx})_{mean} \times d_{sensor}}{E_{pair}} = \frac{(276) \times 500}{3.63} \approx 38.01 \times 10^3 e^- h^+ pair \tag{3.3}$$

The electron-hole pair generated by the incident particle and moving towards the electrode and produce an electric current signal. The current is produced by the moving of charges and is directly proportional to the carrier mobilities according to Ramo,s theorem [22].

$$J_o = \frac{Q_e}{d} \sum u_n + \sum u_p \tag{3.4}$$

where d is the thickness of sensor, Q_e is charge and u_n, u_p is drift velocity of electron and hole.

The total charge can be calculated by taken the integral with respect to time over the induced current:

$$Q_o = \int_0^{t_{int}} J_o dt = \int_0^{t_{int}} \frac{Q_e}{d} (\sum u_n + \sum u_p) dt \tag{3.5}$$

where t_{int} is the integration time of the amplifier. Due to the trapping of charges inside the silicon sensor the measured signal can be reduced. The

Efficiency $\eta_{(CCE)}$ of charge collection is a significant parameter and a subject of interest when analyzing the radiation hardness of a sensor:

$$\eta_{CCE} = \frac{Q_c}{Qo} \tag{3.6}$$

In above equation Q_c is the charge produce in actual calculation and Q_o is total charge.

3.1.2 Mechanical Support Structure and Readout Electronics

A silicon strips module structure as shown in figure 3.1, the mechanical support structure is made by carbon grain fiber and two silicon wafers, readout hybrid and the Kapton Film are installed with high thermal conductivity. The rails are also made by Carbon grain, are glued to both sides of the frame structure. With high accuracy, the pins are fixed at the ends of the structure frame and to align the sensor in the accurate position in the supporting structure. The two wafer strip are joined with each other in such a way that the effective strip-length is 12.5 cm.

The charge from each micro-strip is collected and then amplified by APV25. According to a condition, four or six microchips are combined in the form of hybrid, in order to match hits with collision they contain a lot of information i.e timing, electronic monitoring, temperature etc. For a few microseconds the APV25 stored the signals and then processes them before sending to a laser to convert it into analogs infrared pulses. After these process, the pulses are transmitted by fiber optic cable of 100 m for the analysis in the free radiation environment. Approximately 4×10^4 fibers optic links used in the tracker to provide a low power, the lightweight used to transport the signal. A lot of technology came from the industry [23].

3.2 Silicon Strip Detector APV25 Readout Chip

The APV25 is the micro-strips detector readout chips as shown in figure 3.4. It is the first big chip for an "EHEP" to use as a new commercial 0.25 μm CMOS process. The experimental characterization of the circuit gives a complete functionality and outstanding performance of irradiation before and after the experiment. They contain 128 channels for readout each consists of 50 nanosecond CR-RC types shaping amplifiers. It also has 192 elements rooted pipeline and the final stage are a process of pulses shaping which can be operated in a deconvolution mode which is crucial for the high luminosity [24].

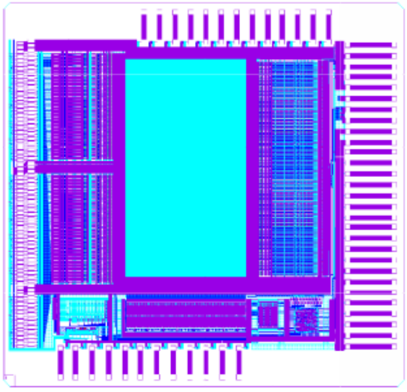

Figure 3.4: CMS silicon strip tracker detector APV25 readout chip.

3.2.1 Front End

The front end area contain pre-amplifier and shaper:

3.2.1.1 Pre-Amplifier

The preamplifier consists of a single-ended cascode CR-RC type shaping amplifiers having 0.15 pF feedback capacitor. The p-channel FET (Field

Effect Transistor) input transistor has a bulk of 2000 μm/0.36 μm and current is 400 μA. In every channel, the pre-amplifier coupled with a shaper amplifier which produces CR-RC pulse shape after every 25 ns, in-between these two gain inverter are placed which as work is a switched. It is introduced in order to operate in both polarities of the signals, they help to prevent the loss of information such that the polarity of the signals at shaper output is the similar either polarity of detector signals.

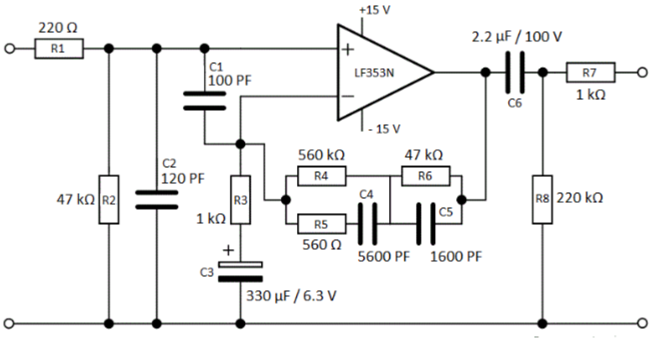

Figure 3.5: Pre-amplifier circuit.

3.2.1.2 Shaper

The shaper is made from the powerful CR-RC filter, it is responsible to produce analog pulse after every 50 ns. The shaper amplifier is working in large range scale, to balance the inevitable degradation of the analog pulse which is produced by irradiation.

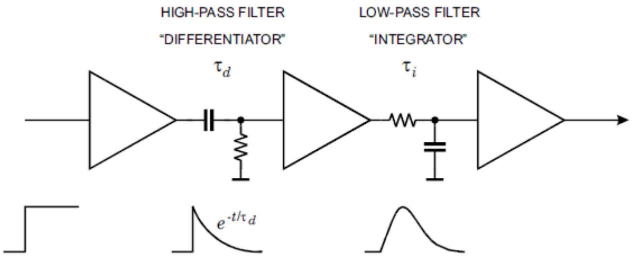

Figure 3.6: CR-RC shaper circuit.

The shaper is formed by a single-ended cascode amplifier with a coupling capacitor 1.4 pF and a feedback capacitor of 150 fF. The bulk of the pFET input transistor is 200 μm /0.36 μm and is bias at 48 μA. The power dissipation of shaper is 0.25 mW, provided the total front-end power dissipation is 1.15 mW and the front end power gain is 100 mV/mip with a non-linearity is less than 2.00% over a 5.00 mip limit. In figure 3.7 it is measured at point "a".

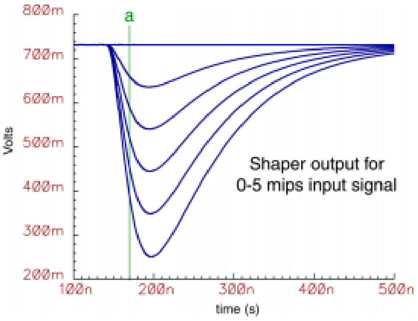

Figure 3.7: Response of shaper.

3.2.2 Pipeline Cell

The pipeline cell contained 128 channels by 192 columns of an on-off capacitor. The outcome of any channel is sampled at 40 MHz shapers into a 192 long pipeline cell. The pipeline cell provides a programmable level one latency up to 4.00 μs, with 32 stations held for buffering events expecting readout. If the microchip is triggered the proper pipeline cell row are selected for read-out process, and not overcome until this is achieved. The analog pulse shaper circuit is used for the readout of pipeline cell channel.

3.2.3 Analog Pulse Shape Processor

The signals coming from the silicon strip detectors and reach to the input of APV25 are consists of single impulses of current which are integrated by preamplifier CR-RC shaped as shown in figure 3.8, then converted into voltage

pulses. These signals are regularly sampled after each 25 ns and then they are saved in the pipeline cell where they are readout.
The APV25 chip can be read out in two different modes, the peak and deconvolution mode. In the peak mode, the only one sample per channel is read out from the cell. The peak mode is operated when the data rates are quite low, such that the outcome of the detector signal that pile-up is not powerful. This mode has a maximum signal-to-noise ratio but the signal has minimum nonlinearity. However, at the higher data rate, the pile-up becomes indicative. In this case, the peak signal is not enough to sample because CR-RC will overlap the shape signals. To overcome this problem, the chip operates in deconvolution mode [25].

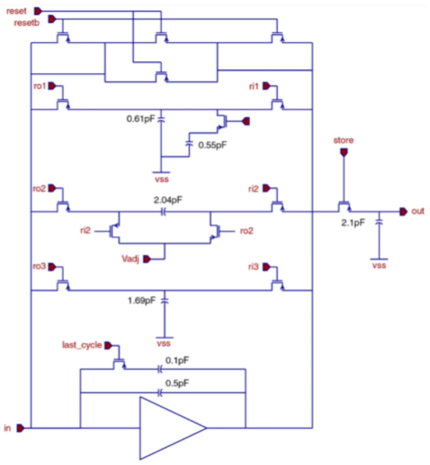

Figure 3.8: APSP system circuit.

In the deconvolution mode three individual samples are combined and take it as a weighted sum of the three signals and then readout by pipeline cell. In the deconvolution mode operation the occurring of a re-shaping of the analog pulse shape and reduce the time taken to 25 ns and returns quickly to the baseline. The third sample corresponds to the voltage at point "a" is given in figure 3.7. The first and second samples corresponding to the voltages at 25 ns and 50 ns respectively. It is necessary to calculate that the original signals are formed. It is deconvoluted in 25 ns. All these processes are executed in the APSP.

Figure 3.8 shown that the analog pulse shaper processor consists of a three weight finite impulse response filter, a charge amplifier and an on-off capacitor circuit. The operating area of the charge amplifier is same as that of shaper and DC coupled to the readout pipeline.

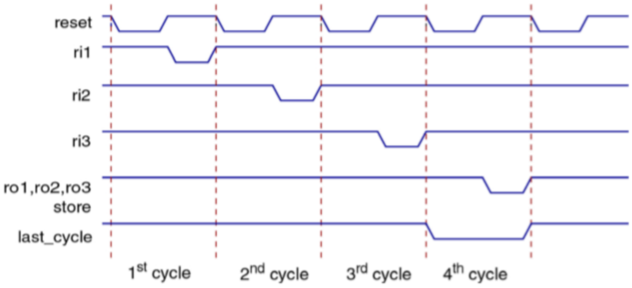

Figure 3.9: Timing of APSP in Deconvolution mode [25].

In deconvolution mode, the APSP working is shown in figure 3.9. From the triggered pipeline cell the charge is readout in the form of series (in case of intense periods of (r_{i1}, r_{i2}, r_{i3})) and integrated onto feed-back capacitor of APSP. The charges saved on this capacitor then add (in case of intense periods of r_{o1}, r_{o2}, r_{o3})) and again the feedback capacitor are integrated, which is now been increased in size $(last_{cycle})$ to decrease the gain of pulses. The capacitor stored the output voltage.

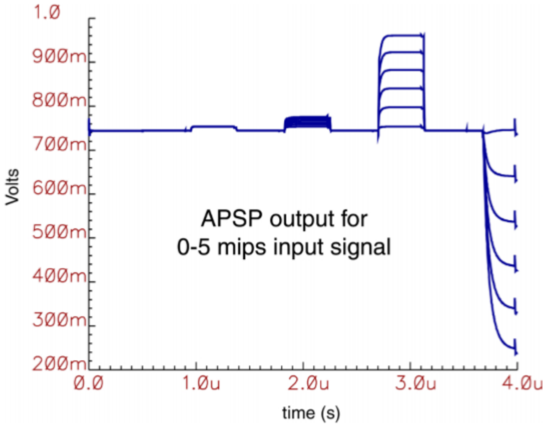

Figure 3.10: The deco mode signals taken from the APSP [25].

In the deconvolution mode, the output working of APSP shown in figure 3.10. If the output shape of signal is perfect CR-RC like shape then the first and second signal is minute as shown in figure 3.10. While the second one showed a small signal. This is due to a small knee in the rising side of the shaper signal, and the weighting of the APSP capacitor. The increased in the complete analog chain up to this point is 100 mV/mip with a non-linearity of less than 2.110% over a 5 mip range.

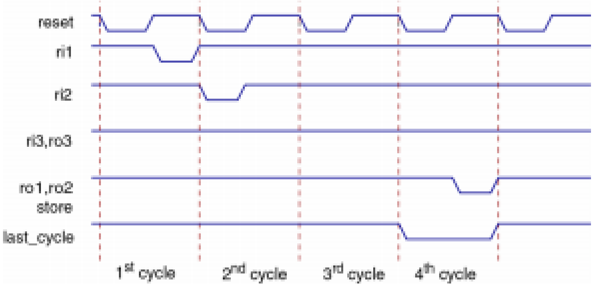

Figure 3.11: Timing of of APSP in Peak mode [25].

In the figure 3.11 shown output signals of APSP in peak mode. From the figure, we can say that the charge stored in one pipeline cell which is read during r_{i1} and integrated onto the APSP feed-back capacitor and the voltage signals are shown on the first of the weighted capacitor. In the period r_{i2}, the APSP reset the level which is sampled onto the second weighted capacitor. These two capacitors stored the charges and added, then integrated on the APSP feedback capacitor (period of r_{o1}, r_{o2}). In the period of signals store, the resulting voltage is sampled on the hold capacitor.

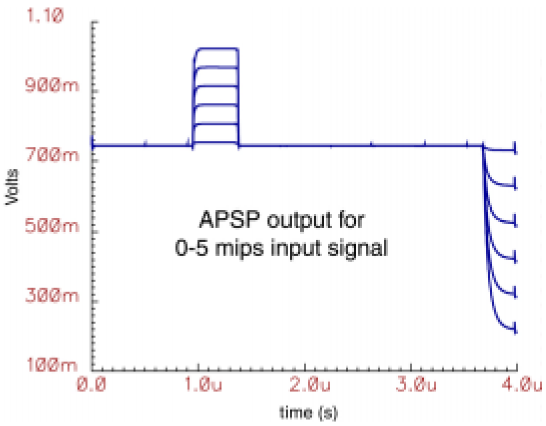

Figure 3.12: Timing of APSP in Peak mode [25].

In the peak mode the operation of APSP is shown in figure 3.12. The output of the complete analog chain up-to this point is 100 mV/mip with a non-linearity of less than 0.6% over a 5 mip range [25]. The Peak mode non-linearity is better compared to deco mode because in deco mode the shaper signal is sampled on the rising edge which may be prone to slewing effects for large signals. The APSP power dissipation is 0.2 mW.

3.3 Particle Path Reconstruction

The CMS detector consists of a high quality hardware parts. The hadron collider also demands from the CMS to handle high standard data. After the proton-proton collision, the data have passed through different trigger level, using the different logarithm to process the raw data and the reconstruction of particles path in the different part of detectors. In the tracker part, it gives to predict and differentiate different hits point or position is shown in the tracker part to find trajectories of a different particle, the ECAL, HCAL detector estimate the energy of particles according to their particular shower shape. The last part of the CMS detector is the muon station which gives stand-alone of muon particles reconstruction and other information about muon. All information is combined from sub-detector to created particles candidate which used for data analysis as shown in figure 3.13.

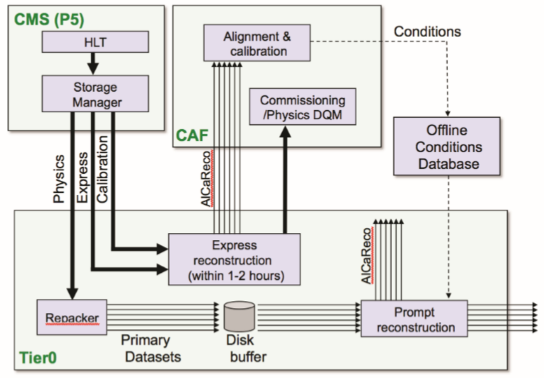

Figure 3.13: In these process the information is collected from all detector to create particle candidate [15].

3.3.1 Track Reconstruction

The combinatorial track finder (CTF) is used at CMS as a track reconstructed algorithm [26]. Three steps are necessary for the track reconstruction, the seed finding, the pattern recognition and the last one track fitting. In the first two steps CTF are used for the capacity of the Kalman Filter(KF) [27].

- Seed Finding: In this step, we find initial points of a probable trajectory.
- Pattern Recognition: In this step, we pointed out different hit association with the trajectory.
- Track Fitting: In this step, we determinate errors and different parameter of trajectory.

3.3.1.1 Seed Finding

Three points are important for the seed finding and the evaluation of the initial point of trajectory framework. If a track corresponds to a collision, the seed finding steps consist of a pair of hits in the innermost layer with an additional beam sports check or triplet hits taken from the inner layers. Firstly, the pixel hits are taken, but if the hits on the pixel layer are missing, then the seed can also be taken the hits from a double-sided module of silicon strip tracker detector. The starting part of the trajectories are a helix-like a trajectories with a maximum curvature, with a least p_t of the track. Some modification had to be done for the cosmic track. Also, the seed taken from outer layers, this for a specific case. When the magnetic field is zero some modifications are needed, because there is no helix like part.

3.3.1.2 Pattern Recognition Procedure

In the pattern recognition, we selected more hits to the track of particles, this is computationally the most absolute part of the reconstruction procedure. Initiated from the first hits, the next all layers are considered. The uncertainty of the track parameter is used to define the width of the search window. Found hits are contentiously joined to the trajectory candidate and each time the track parameters are updated by operating a track fit. In case of missing two alternative hits in consecutive layers which can be assigned to the track, the trajectory is discarded and not propagated any more.

3.3.1.3 Track Fitting Process

In the track fitting step, a Kalman filter is used, which is a progressive least square method. Due to this method, the iteration of χ^2 is the increase of the track based on the difference between the hits and the trajectory state predicted on the surface of a detector. It is pointed with an initial estimation of the track parameters and then summing step by step the hits given by the pattern recognition process. The trajectory of a particle on each layer is determined as a trade-off between the state of current hits and the state which is selected from the previous layer. All information of trajectories state from the previous hits are hold in the last added layer so with each step the accuracy of the state increasing. When all hits are processed, the fit is rerun in the reverse direction and the last trajectory states are given by the combination of both fits in order to benefit from the information of all hits on each surface.

Chapter 4

Shift in the Sensor Position

4.1 Backplane Correction Analysis

The tracker module has operated in two different modes, peak and deconvolution modes [28][29]. The peak mode is used to take the data from the APV25 chip and then save the amplified signals after every 50 ns. Deconvolution mode consists of a weighted sum of three consecutive peak signals, which efficiently decreased the time up to 25 ns. Peak mode is characterized by a good S/N ratio and large integration time, perfect for cosmic data that came into sight at arbitrary times. The peak mode is not acceptable to the high bunch crossing frequency of the hadron collider. Therefore the APV25 chip is operated in deconvolution mode to process data.

4.1.1 Shift of the Read Out mode

The silicon strip detector module can be operated in peak mode for the low data rate i.e cosmic data. In case of collision data, the peak mode is not capable to take the data in 25 ns. The deconvolution modes used to take the collision data, its reduce the readout time up to 25 ns, which correspond to the bunches crossing time [17].

Alignment framework used the similar approach but using either peak or deconvolution mode to take the track from the sensor plane. The alignment framework introduces a shift (Δu) in the local u and w direction in the presence of MF. The shift (Δu) is applied in the sensor position while taking the track in deconvolution mode data. It is corrected to shift (Δu) the sensor position in the local w direction. The value of shift (Δu) for the TOB is reported (In this thesis) using 2017 data of CMS.
Also a few radian shift associated with the Lorentz angle (θ_{LA}). Both shifts (Δu, $\Delta tan(\theta_{LA})$) can be interpreted by a model is known as Venturi model [30], this model illustrates shift of the charge accumulation for the two processing modes. Figure 4.1 shows a charged particles are generated when a track of particles passing through the sensor.

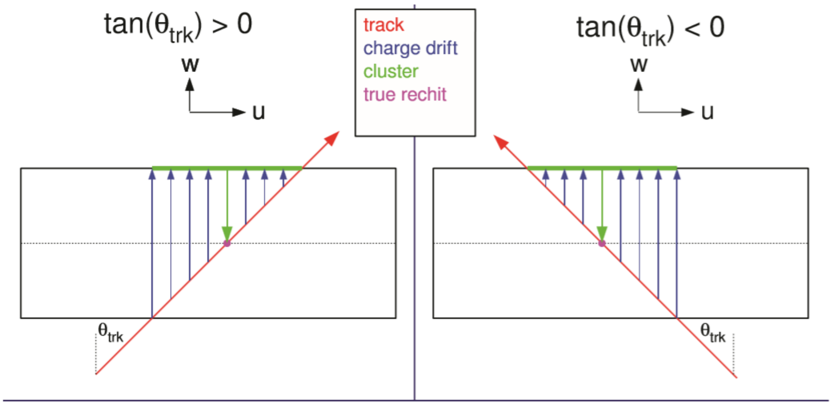

Figure 4.1: A charged particles are generated when the track of particles passing through the sensor plane and these charged particles traversing toward the plane [30].

All charges move towards the plane of the sensor and made a cluster, while they are processing in both modes. The cluster barycenter is hypothesized to the center point of the sensor plane. It is the original reconstructed hit point. In the deconvolution mode, the readout scale of time is small not all charges are accumulated, because the drift time taken the charges to collected from the backplane of the sensor or module is quite large. Therefore, the reconstructed hits point hypothesizes with the cluster barycenter, which is wrong and the alignment framework is adjusted, by shifting position of sensor in w direction such that the reconstructed hits point aligned with the track path (see in figure 4.2).

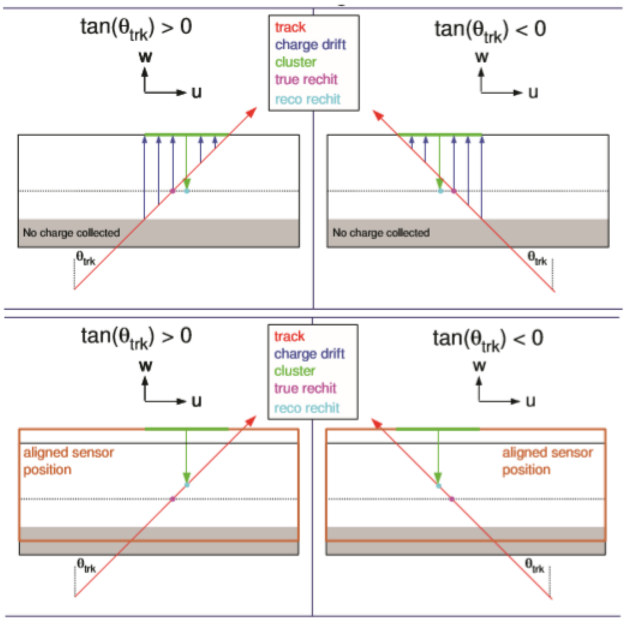

Figure 4.2: In case of deconvolution mode, all charges are not accumulated and the persuasive charge conclusion of a bias of the reconstructed hit points to infer from the clusters barycenter [30].

The above simplified model ignores the description of the Lorentz angle (θ_{LA}), which is also a minute shift in local u direction. Since the integration time for the charge accumulation in deco mode is too small that leads to a minute shift value of the possible Lorentz angle (θ_{LA}). In case of larger times, all charge is accumulated on only single sensor strips. The division of charge between primary and supplementary strips takes a small time. Due to this reason, the possible Lorentz angle is small with respect to the actual one is illustrated in the figure 4.3.

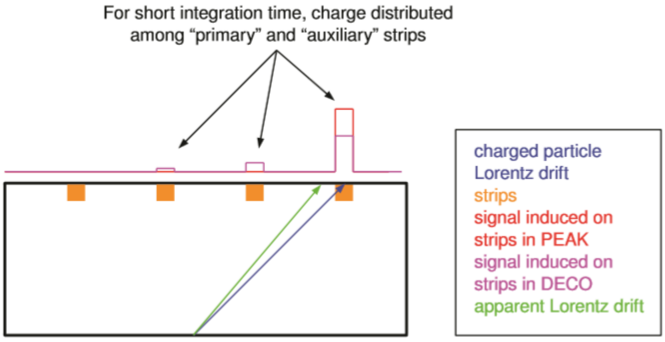

Figure 4.3: The charge cumulation in deco mode gives a smaller value of Lorentz angle [30].

Figure 4.4 shows the adjustment of the u-direction appear from the losses of charge.

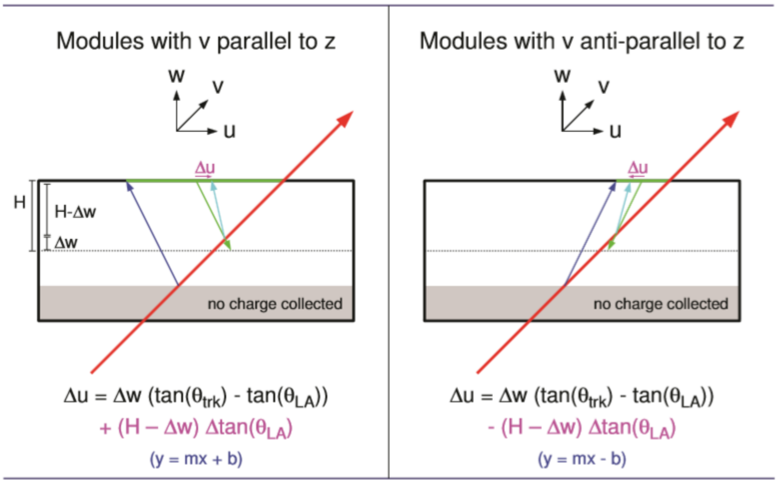

Figure 4.4: Losses of charge in deco mode gives a value of Lorentz angle, the actual value is greater than from the possible Lorentz angle [30].

The term originating from the unknown accumulated charges of the back-plane $\Delta w(tan\theta_{trk}$ - $tan\theta_{LA})$ are drawn out by the adjustment of a lesser effective value of Lorentz angle (θ_{LA}) shown at the drift length $H - \Delta w$. Both shift necessary to be achieved in case of locally reconstructed hits to support unbiased clusters and thus unbiased reconstructed hits point of the alignment. The Lorentz angle (θ_{LA}) shift is only significant for the outer barrel as the shift is not important in the thinner inner barrel modules. It is measured to be 0.013 radians [30].

4.1.2 In Case of Zero Magnetic Field

It was reported, that for the deconvolution mode data the sensor position has shifted with respect to sensors positions in the peak mode. The sensor position has shifted from its original positions towards the align sensor position, the order of shift was orthogonal to the plane of the sensor as shown in figures 4.5 4.6 and in the direction of Lorentz drift.

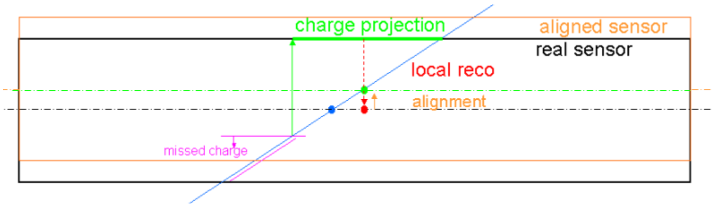

Figure 4.5: In the absence of magnetic field the position of the sensor in both cases, one is the original and the other is shifted geometry of the sensor [30].

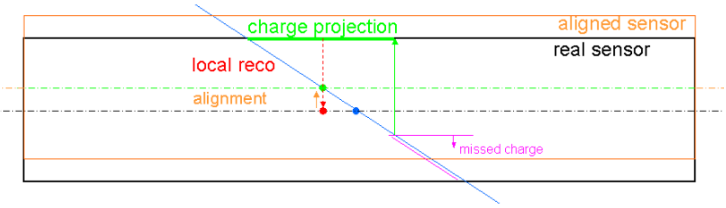

Figure 4.6: In the absence of magnetic field the position of the sensor in both cases, one is the original and the other is shifted geometry of the sensor [30].

The blue line and the point representing the track and the barycenter of the tracks on the sensor plane. The purple line representing the track is due to the loss of charge and the green point represent the barycenter of that lost charge. These charge drifts along the electric field as results green clusters are created. The use of local reconstruction, this cluster is reconstructed as red point. After reconstructions, the barycenter of cluster is converted back to the expected drift direction. Therefore, an imbalance occurs between track, green point and the reconstructed hit, red point. To recover the imbalance, an alignment process is apply which shift the sensor along the orange arrow in a direction orthogonal to the sensor plane and by doing that a Δu shift is introduced.

4.1.3 In Case of Magnetic Field

In the presence of a magnetic field, the shift is observed in two directions, one is orthogonal to the sensor plane and the other is parallel to the direction of the sensors plane.

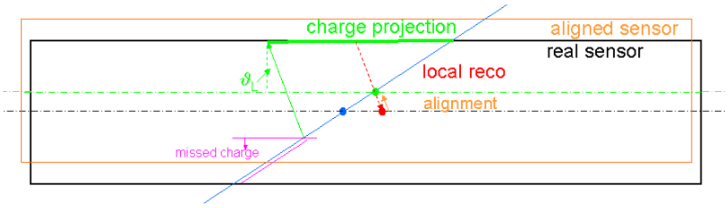

Figure 4.7: In the presence of magnetic field the position of the sensor in both cases, one is the original and the other is shifted geometry of the sensor [30].

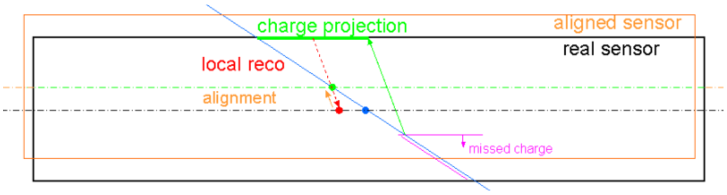

Figure 4.8: In the presence of magnetic field the position of the sensor in both cases, one is the original and the other is shifted geometry of the sensor [30].

4.1.4 Measurement of Lorentz Angle

In case of magnetic field, the Lorentz force acts on charges which are displaced from its path, this displacement is proportional to their drift length. The depth at which charge carrier is created (along z (local coordinate)) and their displacement which is along x (local coordinate) direction, is estimated by track variable of traversing track. The contracted depth should have large measurement points, for this purpose, the cluster should be along y (local coordinate) direction which leads to trivial (grazing) impact track angle β as sketched in figure 4.9.

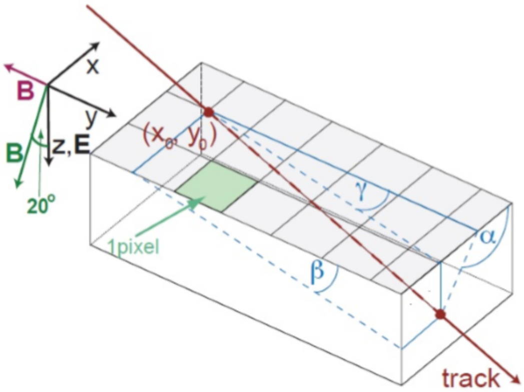

Figure 4.9: In deconvolution mode the charges loses that leads to an effective Lorentz angle.

The depth of charge carriers are taken as a function of mean shift, and from the slope the tangent of the Lorentz angle is measured. The trajectory to each layer of the detector is extrapolated to measure the strike point (x_o, y_o) of the track on the surface of the strip sensor. Each strip sensor collects the charge which is then calculated as a function of the strike point of the track and the distance between the given strip. The distance between two points are:

$$\Delta x = x - x_o, \Delta y = y - y_o \tag{4.1}$$

The charge is calculated for the central part of the strip detector (x_o, y_o). The following relation is used to get impact track angle

$$tan\alpha = \frac{P_z}{P_x}, tan\beta = \frac{P_z}{P_y}, tan\gamma = \frac{P_x}{P_y}, \tag{4.2}$$

where P_x, P_y, P_z show the component of P_{track} in the local coordinate system. The depth z of ionization charges and displacement d is given by

$$d = (\Delta x - \Delta y).tan\gamma, z = \Delta y.tan\beta \tag{4.3}$$

Finally, the Lorentz angle can be measured from the ratio of charges displacement and their depth

$$tan(\theta_{LA}) = \frac{d}{z} \tag{4.4}$$

Chapter 5

Shift Measurement and Optimization of Selection Criteria

In this analysis, we used the CMS 2017 collision data taken from the peak and deconvolution mode respectively. The alignment framework uses either track or hits taken in peak or deconvolution mode of data. This framework has introduced a shift (Δu) in the sensor position as well as in the Lorentz angle of deconvolution mode. These shifts are briefly explained in chapter 4. In this chapter, the shifts (Δu, $\Delta tan(\theta_{LA})$) introduce by the alignment framework have been measured. The shift (Δu) in the sensor position of the inner barrel (TIB) was reported as a few microns. The value of shifts (Δu) in the sensor position and $\Delta tan(\theta_{LA})$ for the tracker outer barrel (TOB) are described below.

5.1 Backplane Correction

The local coordinate are associated with each sensor plane which are represented by u (local z coordinate), v (local y coordinate) and w (local x coordinate) coordinates. The w coordinate is orthogonal to the sensor plane and u, v are in the sensor plane making 90^o angle with each other. The silicon strip detector consist of 15,148 highly sensitive module readout by APV25 chips. The APV25 chips can be operated in different modes, which are peak and deconvolution mode. Alignments framework use the similar approach but using either peak or deconvolution mode data to take the hits. An alignment would be applied when the hits have been taken in the deconvolution mode. The shift in the sensor position explained in section (4.2), in case of magnetic field the shift will be in two directions w and u.

5.1.1 One Dimension Distribution of Shift

The alignment framework is used to take the track or hits of particles from the different layers of TOB. In the deconvolution mode the alignment framework introduces a shift in the sensor position with respect to the peak mode. This shift are explained by two variables local x and rhlocal x. The local x variable associated with the real sensor position and reconstructed local x variable associated with the align sensor position in the software framework (related with reconstructed hits). The shift is defined by:

$$Shift = localx - rhlocalx \tag{5.1}$$

5.1.2 Local x-Variable

The local x variable related with track and hits in the real sensor position as shown in figure 4.5 with the blue point and blue line. In figure 4.5 the real position of the sensor is shown with the black line. The distribution of the local x variable as shown in figure 5.1 for different layers (6-layers) of TOB. Similar distributions are plotted for peak mode.

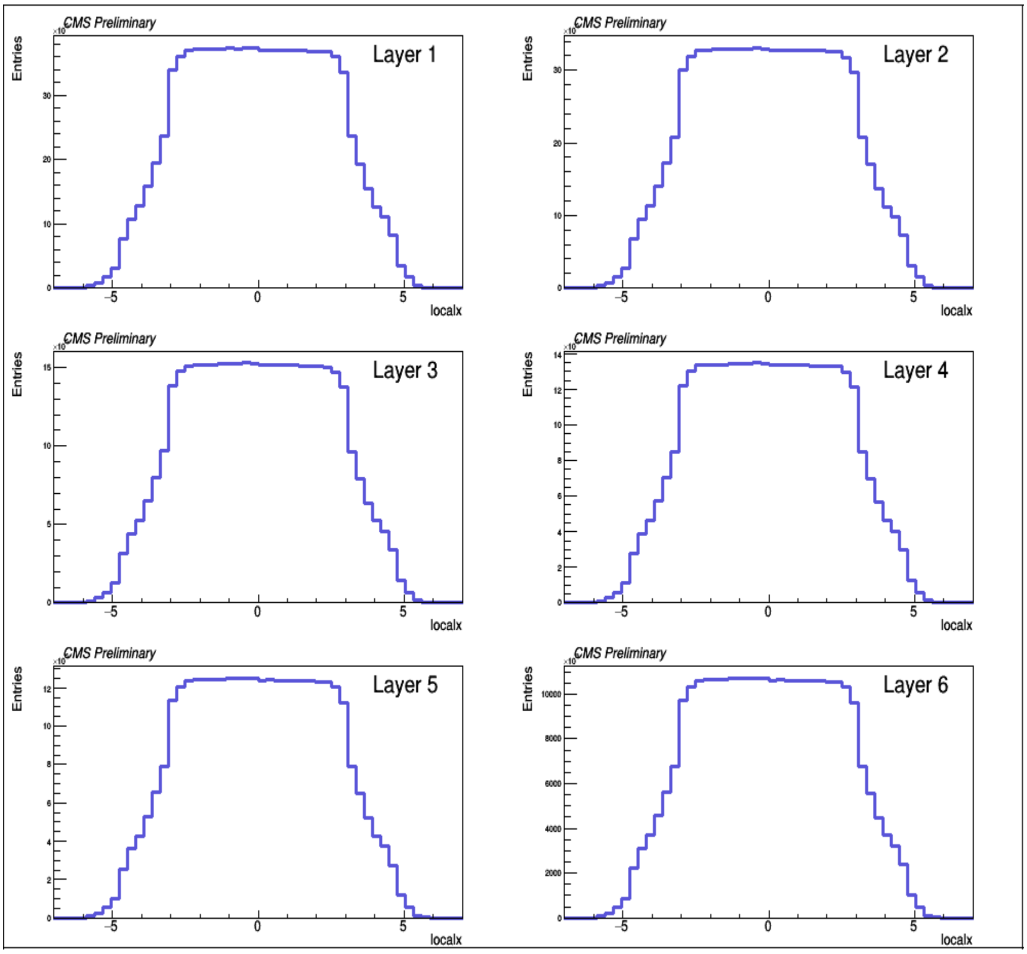

Figure 5.1: The deconvolution mode distribution of local x variable for different layers of tracker outer barrel (TOB).

5.1.3 Reconstructed Local x-Variable

The reconstructed local x (rhlocalx) variable is related with reconstructed tracks and hits. The aligned sensor position is represented by green point and purple line as shown in figure 4.5. The position of aligned sensor is represented by coral color as shown in figure 4.5. The distribution of the reconstructed local-x variable is shown in figure 5.2 for different layers (6-layers) of TOB.

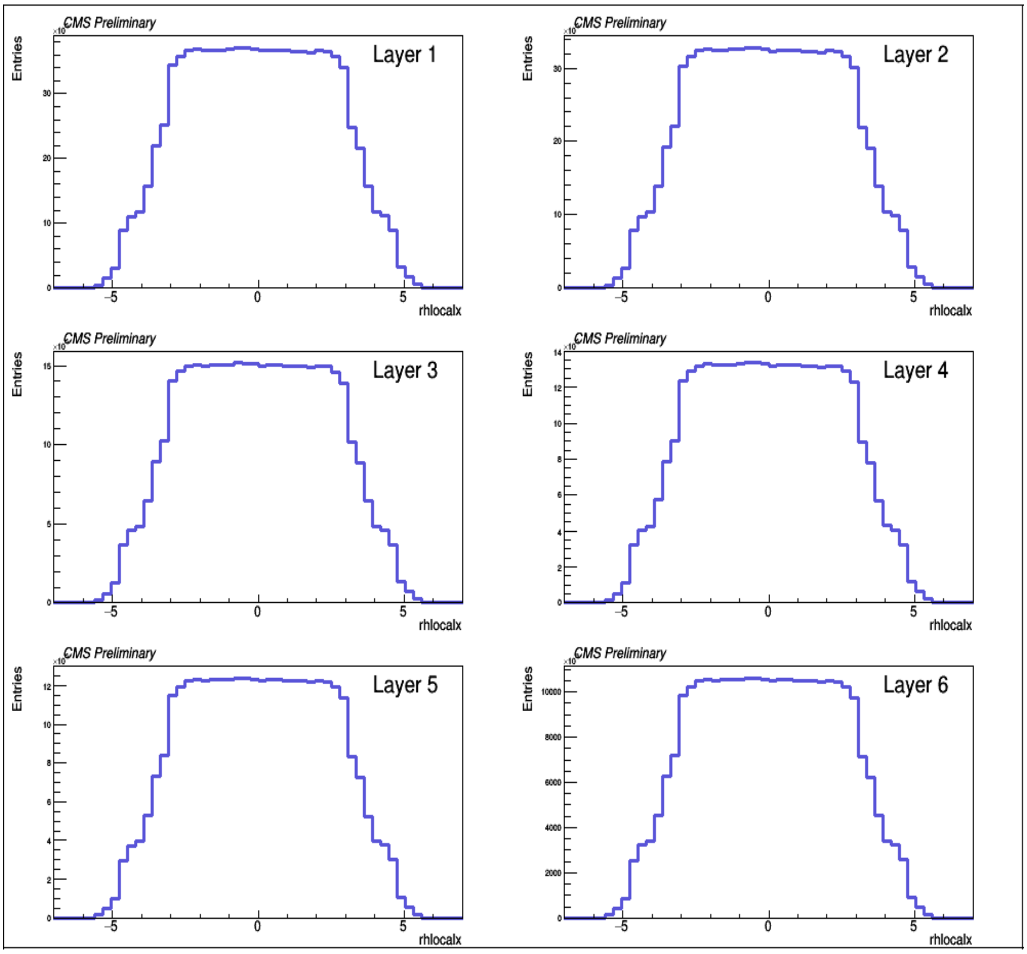

Figure 5.2: The deconvolution mode distribution of reconstructed local-x variable for different layer of tracker outer barrel.

The difference between local-x and reconstructed local-x (rhlocalx) is defined by shift. For different layers of TOB the one dimension distribution of shift is shown in figure 5.3. To find the backplane correction we plotted tan(θ_{trk}) vs shift.

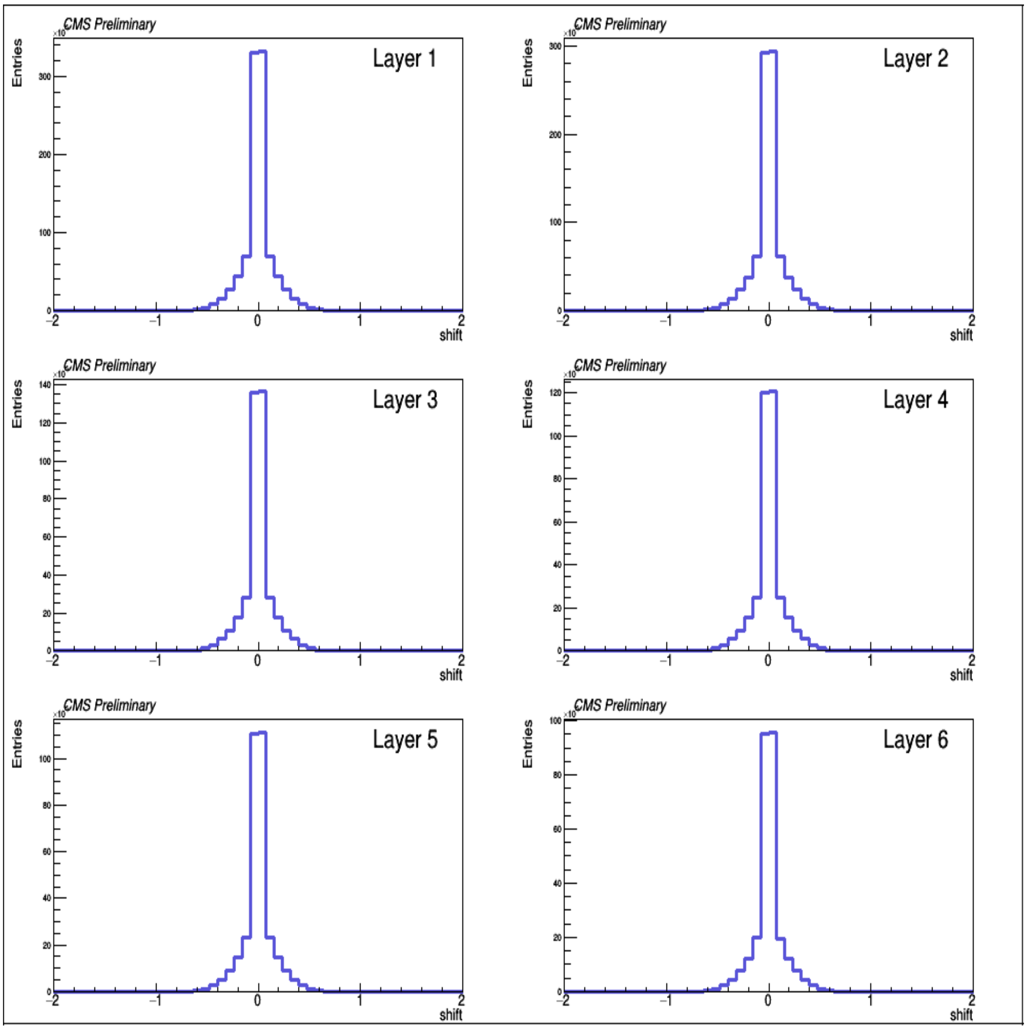

Figure 5.3: One dimension distribution of shift for six layers of TOB.

5.2 Selection Criteria for Track Momentum ($\mathbf{P_{trk}}$)

The silicon strip tracker (TOB) is the outer part of the tracker detector, that consists of six layers of different radius. The first layer of it is to close to the interaction point. Then after this the second layer is installed and so on up to six layers. For the measurement of backplane correction, we here applied some cuts criteria on track momentum. The track momentum ($\mathbf{P_{trk}}$) is the important parameter of the tracks of particles. The first criterion on the track momentum is **0.8 GeV** and the second criterion is **1.5 GeV**. These criterion help us to understand that in the first criterion we block all tracks which have the track momentum is less than **0.8 GeV** because the low momentum tracks pass through the first layer but these low momentum track did not pass through the far away layers of TOB.

Since low ($\mathbf{P_{trk}}$) tracks are bounded by first layer. The second criterion is (**1.5 GeV**) used for the improvement of tracks to pass from all layers of TOB. In this thesis, we applied these two cuts to reported the backplane correction. The one dimensional distribution of track momentum for six layers of TOB is shown in the figures (5.4, 5.5, 5.6, 5.7, 5.8, 5.9).

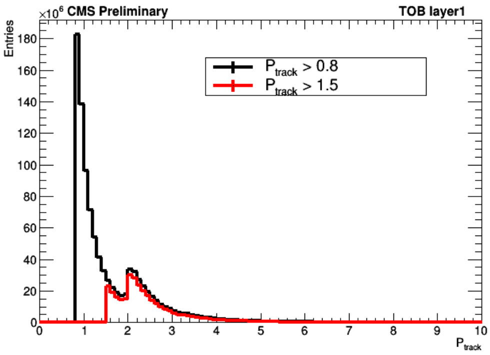

Figure 5.4: The track momentum with cuts 0.8 GeV (black) and 1.5 GeV (red) for layer 1.

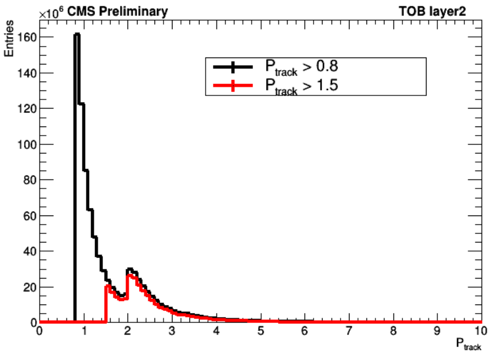

Figure 5.5: The track momentum with cuts 0.8 GeV (black) and 1.5 GeV (red) for layer 2.

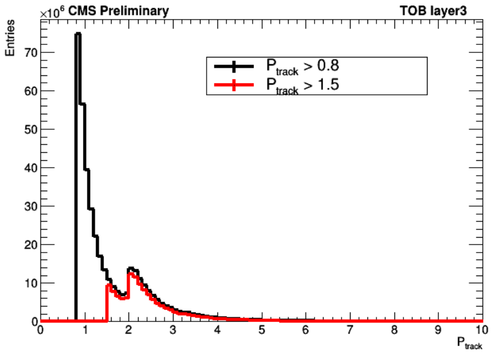

Figure 5.6: The track momentum with cuts 0.8 GeV (black) and 1.5 GeV (red) for layer 3.

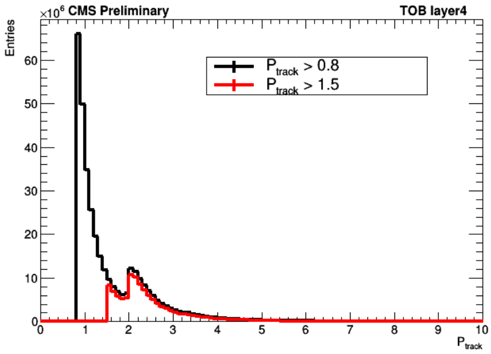

Figure 5.7: The track momentum with cuts 0.8 GeV (black) and 1.5 GeV (red) for layer 4.

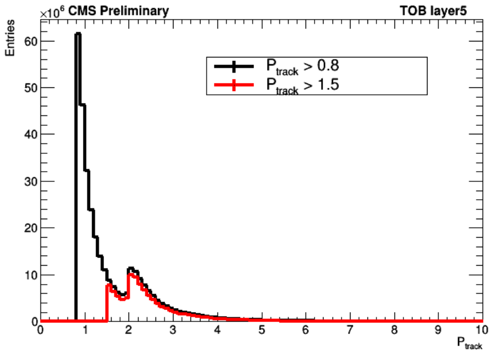

Figure 5.8: The track momentum with cuts 0.8 GeV (black) and 1.5 GeV (red) for layer 5.

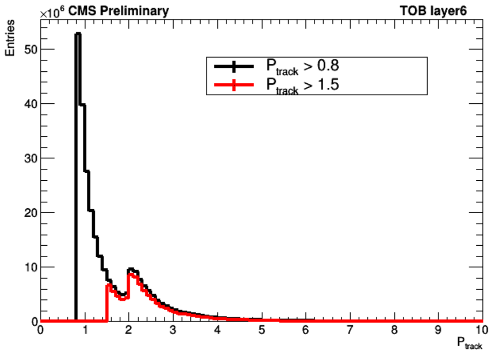

Figure 5.9: The track momentum with cuts 0.8 GeV (black) and 1.5 GeV (red) for layer 6.

5.2.0.1 The Backplane Correction (Δw)

In this section, we plotted shift vs $\tan(\theta_{trk})$ for both peak and deconvolution modes data respectively. The shift and $\tan(\theta_{trk})$ are given by:

$$Shift = Localx - rhLocalx \tag{5.2}$$

$$Tan(\theta_{trk}) = \frac{X_{Localdirection}}{Z_{Localdirection}} \tag{5.3}$$

In the above equation, the shift is the difference between the local-x variable which is associated with real sensor position and the rhlocal-x variable which is associated with aligned sensor position. The $\tan(\theta_{trk})$ is ratio between local x variable and local z variable. Figure 5.10 shows that the shift is plotted vs $\tan(\theta_{trk})$ for the first layer of TOB, the blue data point show the sensor position while the APV25 is operated in deconvolution mode. Similarly, the red data point shows the sensor position while the APV25 chip is operated in the peak mode. For the other layers is shown in figures (5.11, 5.12, 5.13, 5.14, 5.15).

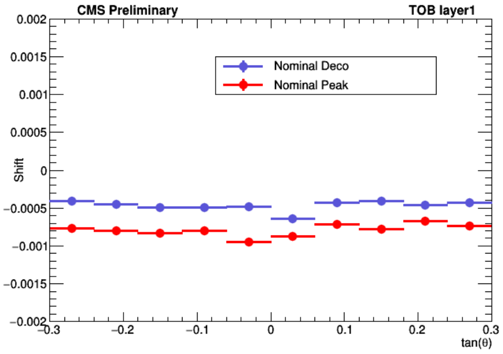

Figure 5.10: The shift vs $tan(\theta_{trk})$ for TOB layer 1, the blue data point shows deconvolution and the red one shows peak mode data point.

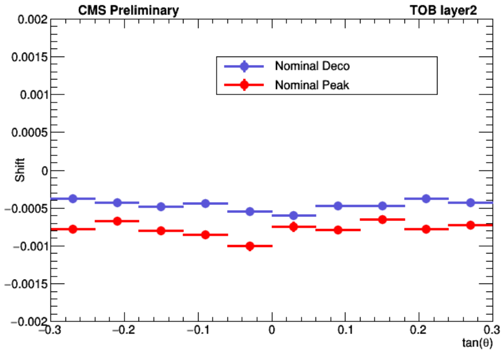

Figure 5.11: The shift vs $tan(\theta_{trk})$ for TOB layer 2, the blue data point shows deconvolution and the red one shows peak mode data point.

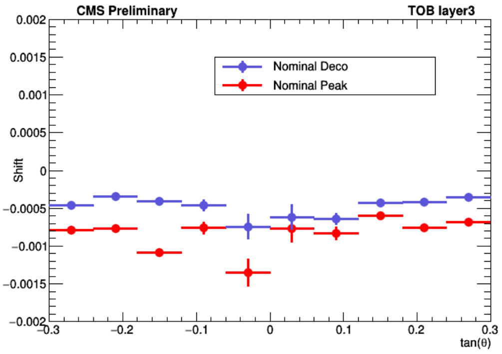

Figure 5.12: The shift vs $tan(\theta_{trk})$ for TOB layer 3, the blue data point shows deconvolution and the red one shows peak mode data point.

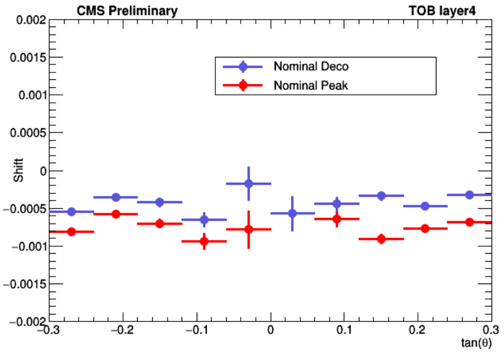

Figure 5.13: The shift vs $tan(\theta_{trk})$ for TOB layer 4, the blue data point shows deconvolution and the red one shows peak mode data point.

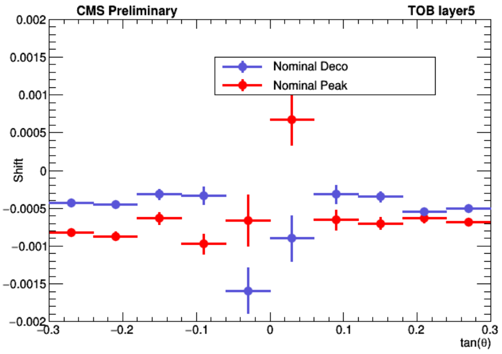

Figure 5.14: The shift vs $tan(\theta_{trk})$ for TOB layer 5, the blue data point shows deconvolution and the red one shows peak mode data point.

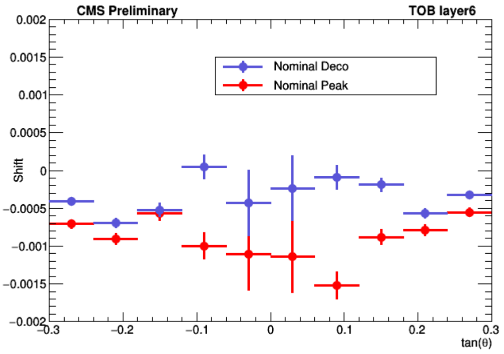

Figure 5.15: The shift vs $tan(\theta_{trk})$ for TOB layer 6, the blue data point shows deconvolution and the red one shows peak mode data point.

To measure the value of backplane correction (Δw) and $\Delta tan(\theta_{LA})$ for six layers of TOB with the implementation of $\mathbf{P_{trk} > 0.8\ GeV}$. The procedure adopted to report the value of the backplane correction, the Δu (shift in the sensor position) is the difference between the shift measured from the deconvolution mode and peak mode.

$$\Delta u = Shift_{(deco)} - Shift_{(peak)} \tag{5.4}$$

The values of backplane correction (Δw) and $\Delta tan(\theta_{LA})$ is calculated from the following equation:

$$\Delta u = \Delta w(tan(\theta_{trk}) - tan(\theta_{LA})) + (H - \Delta w)\Delta tan(\theta_{LA}) \tag{5.5}$$

In the above equation the value MF is H = 3.8 T, $tan(\theta_{LA}) = 0.38$ because $\theta_{LA} = 21^o$. From Δu we found the backplane correction to apply the straight line fit $y = mx + c$. The slope of the straight line fit is the value of backplane correction is shown in the figures (5.16, 5.17, 5.18, 5.19, 5.20, 5.21).

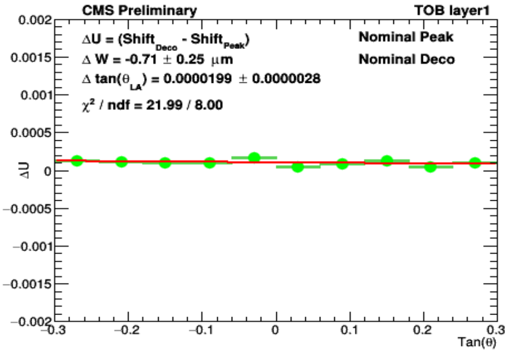

Figure 5.16: The value of backplane corrections (Δw and $\Delta tan(\theta_{LA})$) are estimated by applying the straight fit on Δu for the TOB layer 1.

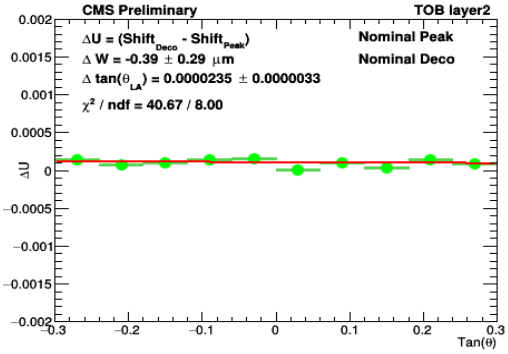

Figure 5.17: The value of backplane corrections Δw and $\Delta tan(\theta_{LA})$ are estimated by applying the straight fit on Δu for the TOB layer 2.

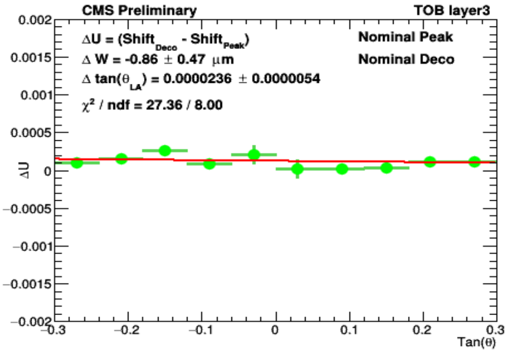

Figure 5.18: The value of backplane corrections Δw and $\Delta tan(\theta_{LA})$ are estimated by applying the straight fit on Δu for the TOB layer 3.

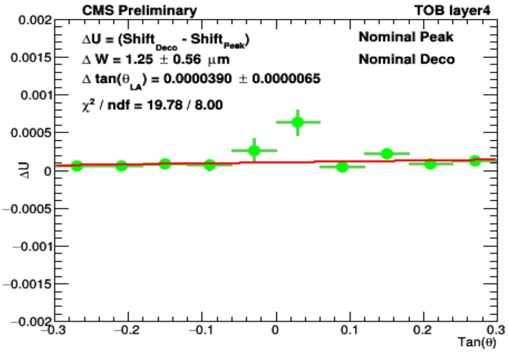

Figure 5.19: The value of backplane corrections Δw and $\Delta tan(\theta_{LA})$ are estimated by applying the straight fit on Δu for the TOB layer 4.

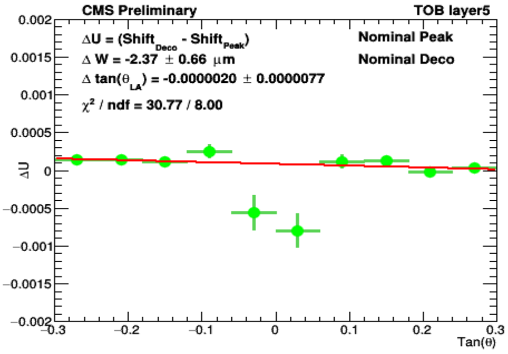

Figure 5.20: The value of backplane corrections Δw and $\Delta tan(\theta_{LA})$ are estimated by applying the straight fit on Δu for the TOB layer 5.

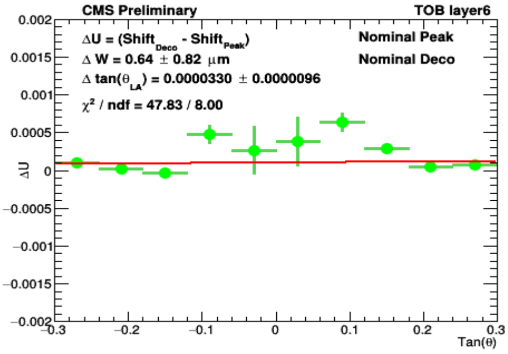

Figure 5.21: The value of backplane corrections Δw and $\Delta tan(\theta_{LA})$ are estimated by applying the straight fit on Δu for the TOB layer 6.

In the table 5.1 the value of Δw, $\Delta tan(\theta_{LA})$ and goodness of fit value are shown for the six layers of TOB.

Table 5.1: The value of backplane correction (Δw) for the different layers of TOB.

No	Δw	$\Delta tan(\theta_{LA})$	χ^2**/ndf**
Layer 1	-0.71±0.25μm	0.0000199±0.0000028	21.99/8.00
Layer 2	-0.39±0.29μm	0.0000235±0.0000033	40.67/8.00
Layer 3	-0.86±0.47μm	0.0000236±0.0000054	27.36/8.00
Layer 4	1.25±0.56μm	0.0000390±0.0000065	19.78/8.00
Layer 5	-2.37±0.66μm	0.0000020±0.0000077	30.77/8.00
Layer 6	0.64±0.82μm	0.0000330±0.0000096	47.83/8.00

In the table 5.1 the value backplane correction (Δw) in the sensor position for the different layers is shown. The shifts in the sensor position as well as in the Lorentz angle are a few microns.

The implementation of second criterion of the track momentum $\mathbf{P_{trk} > 1.5}$ **GeV**, we measured the value of backplane correction for six layers of TOB. A similar procedure adopted to report the value of the backplane correction. From Δu we found the backplane correction to apply the straight line fit. The slope of the straight line fit is the value of backplane correction (Δw) is shown in the figures (5.22, 5.23, 5.24, 5.25, 5.26, 5.27).

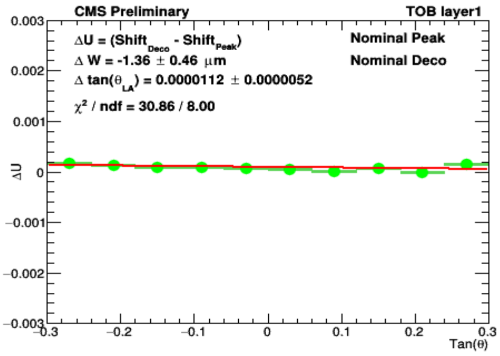

Figure 5.22: The value of backplane correction Δw and $\Delta tan(\theta_{LA})$ are estimated by applying the straight fit on Δu for the TOB layer 1 .

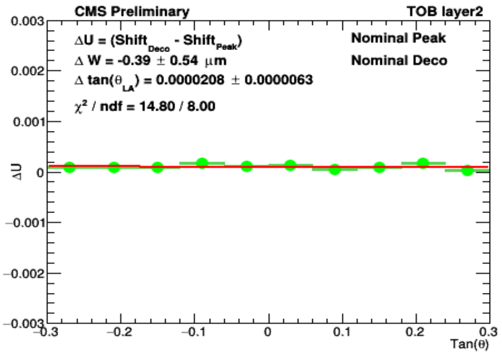

Figure 5.23: The value of backplane correction Δw and $\Delta tan(\theta_{LA})$ are estimated by applying the straight fit on Δu for the TOB layer 2.

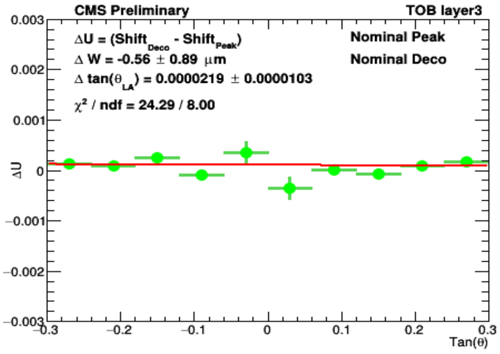

Figure 5.24: The value of backplane correction Δw and $\Delta tan(\theta_{LA})$ are estimated by applying the straight fit on Δu for the TOB layer 3.

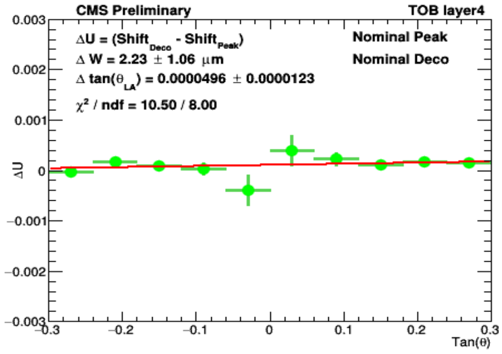

Figure 5.25: The value of backplane correction Δw and $\Delta tan(\theta_{LA})$ are estimated by applying the straight fit on Δu for the TOB layer 4.

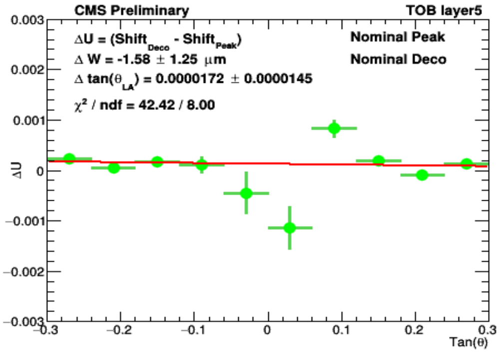

Figure 5.26: The value of backplane correction Δw and $\Delta tan(\theta_{LA})$ are estimated by applying the straight fit on Δu for the TOB layer 5.

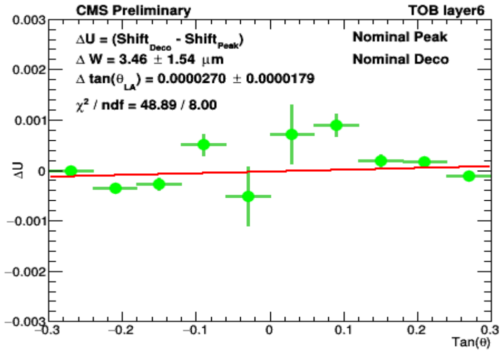

Figure 5.27: The value of backplane correction Δw and $\Delta tan(\theta_{LA})$ are estimated by applying the straight fit on Δu for the TOB layer 6.

In the table 5.2 the values of Δw and $\Delta tan(\theta_{LA})$ are shown for the six layers of TOB. The goodness of fit value is also shown in table for all layers.

Table 5.2: Table of backplane correction Δw, the value of shift in sensor position for the six layers of TOB.

No	Δw	$\Delta tan(\theta_{LA})$	χ^2**/ndf**
Layer 1	-1.36±0.46μm	0.0000112±0.0000052	30.86/8.00
Layer 2	-0.39±0.54μm	0.0000208±0.0000063	14.80/8.00
Layer 3	-0.56±0.89μm	0.0000219±0.0000103	24.29/8.00
Layer 4	2.23±1.06μm	0.0000496±0.0000123	10.50/8.00
Layer 5	-1.58±1.25μm	0.0000172±0.0000145	42.42/8.00
Layer 6	3.46±1.54μm	0.0000270±0.0000179	48.89/8.00

In the table 5.2 the value of backplane correction Δw in the sensor position for the different layers is shown.

5.2.0.2 Optimization of Cuts

From the implementations of both cuts we concluded that the average value of backplane correction (Δw) came from the cut $P_{track} > 0.8$ GeV is 1.03± 0.50 μm with the relative error 48.5%. The average value of backplane correction (Δw) came from the cut $P_{track} > 1.5$ GeV is 1.59± 0.95 μm with the relative error 59.7%. From these result we concluded that the cut on track momentum $P_{track} > 0.8$ is better than from the cut $P_{track} > 1.5$ GeV. We validated the result with $P_{track} > 0.8$ GeV cut.

5.2.0.3 Validation of Result

For the validation of result, we applied the official backplane correction numbers in the code to generate the local-x and rhlocal-x variable, which is called the miscalibration of local-x and rhlocal-x.

The miscalibration means that the sensor position is aligned to its original positions and ideally there should be a few microns backplane correction Δw.

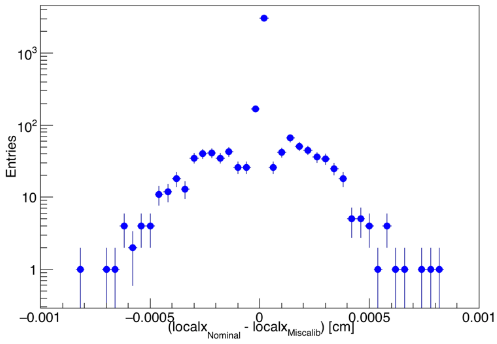

Figure 5.28: The difference between nominal local-x and miscalibrate local-x.

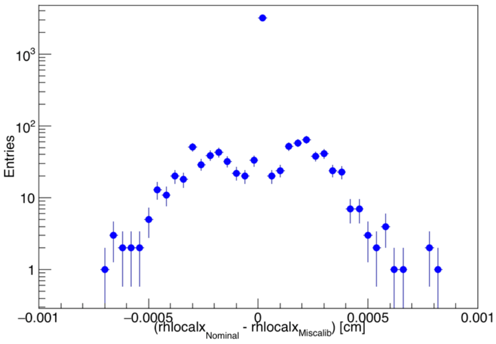

Figure 5.29: The difference between nominal rhlocal-x and miscalibrate rhlocal-x.

The miscalibration is quite small which is in fact a few micron. In the figure 5.28 is shown the difference between nominal local-x and miscalibration local-x. Similarly in the figure 5.29 is shown the difference between nominal rhlocal-x and miscalibrate rhlocal-x.

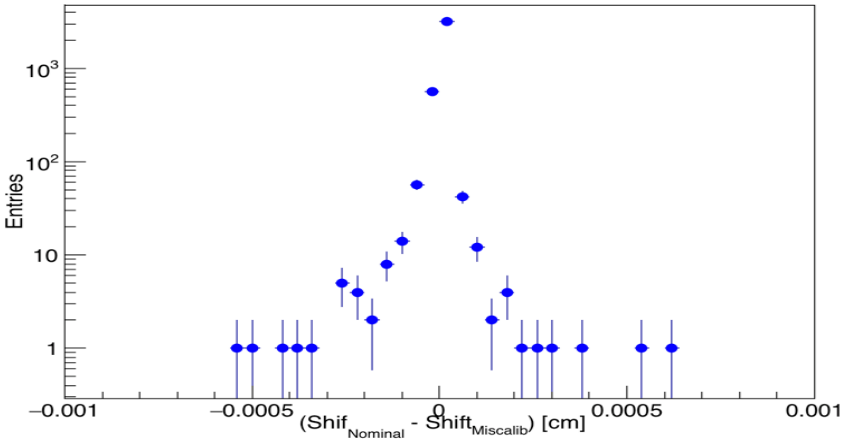

Figure 5.30: The difference between nominal shift and miscalibrate shift.

The difference between nominal shift and miscalibrate shift is shown in the figure 5.30. In the following plots, we plotted the $tan(\theta_{trk})$ vs $shift$ for the peak mode data. Here we also observed a small difference between nominal and miscalibrate peak, which was expected. In the figure (5.31, 5.32, 5.33, 5.34, 5.35, 5.36), shows the overlapping of nominal and miscalibrate peak.

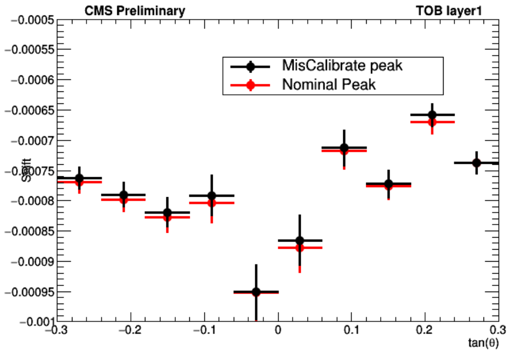

Figure 5.31: The $shift$ vs $tan(\theta_{trk})$ for TOB layer 1, the red data point shows nominal peak and the black one shows miscalibrate peak mode data point.

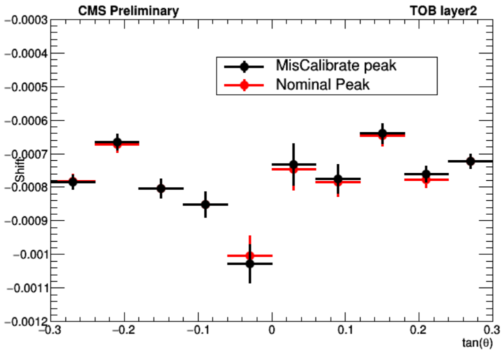

Figure 5.32: The $shift$ vs $tan(\theta_{trk})$ for TOB layer 2, the red data point shows nominal peak and the black one shows miscalibrate peak mode data point.

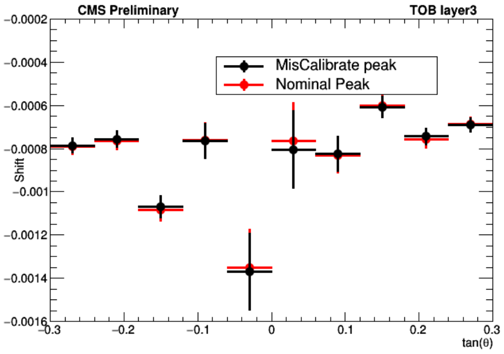

Figure 5.33: The $shift$ vs $tan(\theta_{trk})$ for TOB layer 3, the red data point shows nominal peak and the black one shows miscalibrate peak mode data point.

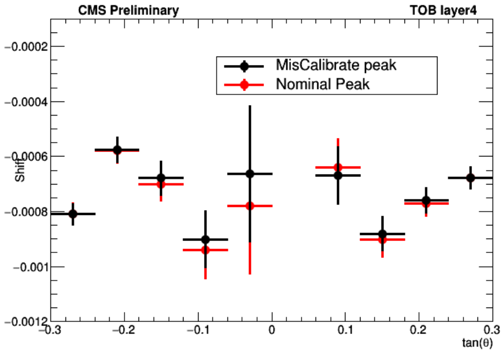

Figure 5.34: The $shift$ vs $tan(\theta_{trk})$ for TOB layer 4, the red data point shows nominal peak and the black one shows miscalibrate peak mode data point.

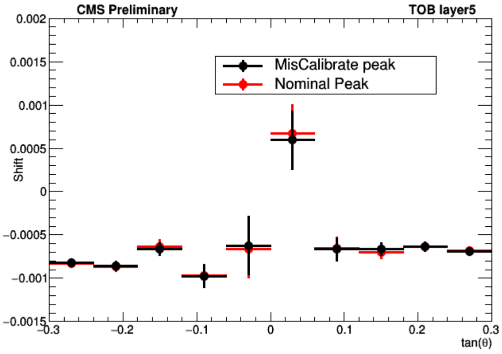

Figure 5.35: The *shift* vs $tan(\theta_{trk})$ for TOB layer 5, the red data point shows nominal peak and the black one shows miscalibrate peak mode data point.

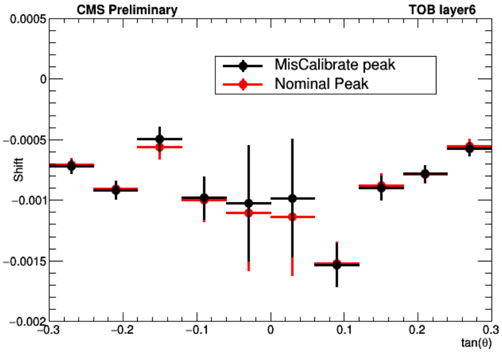

Figure 5.36: The *shift* vs $tan(\theta_{trk})$ for TOB layer 6, the red data point shows nominal peak and the black one shows miscalibrate peak mode data point.

In the following plot the value of the backplane correction is measured with miscalibrate peak mode and the nominal deco mode data. Shown in the figures (5.37, 5.38, 5.39, 5.40, 5.41, 5.42).

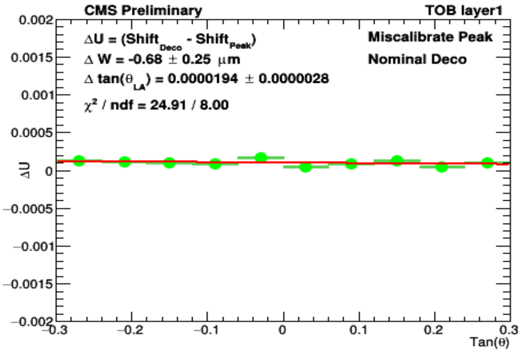

Figure 5.37: The value of backplane correction Δw and $\Delta tan(\theta_{LA})$ for the TOB layer 1. For the validation of result we used miscalibrate peak and nominal deconvolution mode data.

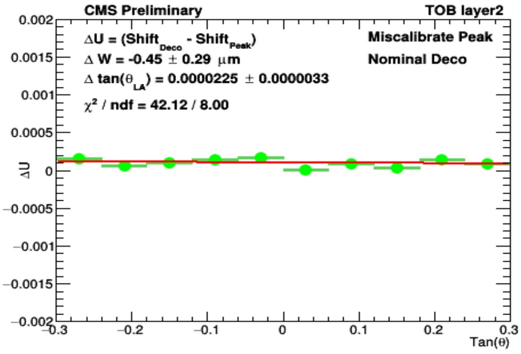

Figure 5.38: The value of backplane correction Δw and $\Delta tan(\theta_{LA})$ for the TOB layer 2. For the validation of result we used miscalibrate peak and nominal deconvolution mode data.

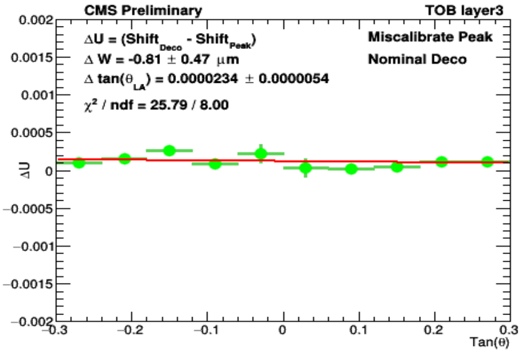

Figure 5.39: The value of backplane correction Δw and $\Delta tan(\theta_{LA})$ for the TOB layer 3. For the validation of result we used miscalibrate peak and nominal deconvolution mode data.

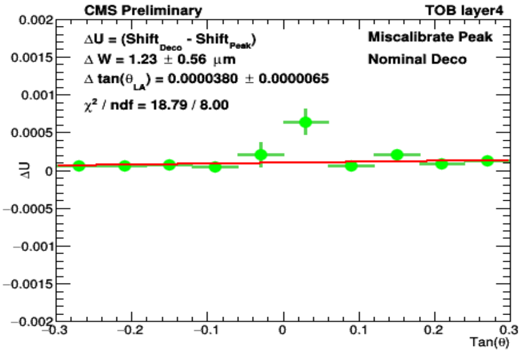

Figure 5.40: The value of backplane correction Δw and $\Delta tan(\theta_{LA})$ for the TOB layer 4. For the validation of result we used miscalibrate peak and nominal deconvolution mode data.

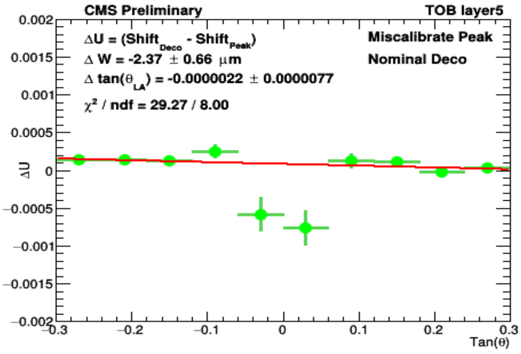

Figure 5.41: The value of backplane correction Δw and $\Delta tan(\theta_{LA})$ for the TOB layer 5. For the validation of result we used miscalibrate peak and nominal deconvolution mode data.

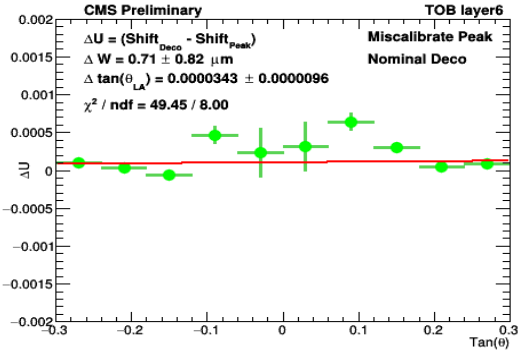

Figure 5.42: The value of backplane correction Δw and $\Delta tan(\theta_{LA})$ for the TOB layer 6. For the validation of result we used miscalibrate peak and nominal deconvolution mode data.

Table 5.3: Table of backplane correction Δw, the value of shift in sensor position for the six layers of TOB. For the validation of result we used miscalibrate peak and nominal deconvolution mode.

No	Δw	$\Delta tan(\theta_{LA})$	χ^2/**ndf**
Layer 1	-0.68±0.25μm	0.0000194±0.0000052	24.91/8.00
Layer 2	-0.45±0.29μm	0.0000225±0.0000033	42.12/8.00
Layer 3	-0.81±0.47μm	0.0000234±0.0000054	25.79/8.00
Layer 4	1.23±0.56μm	0.0000380±0.0000065	18.79/8.00
Layer 5	-2.37±0.66μm	0.0000022±0.0000077	29.27/8.00
Layer 6	0.71±0.82μm	0.0000343±0.0000096	49.45/8.00

In the table 5.3 the value of backplane correction Δw are shown for the different layers of TOB.

5.3 Conclusion

The value of backplane corrections (Δw) and shift in the Lorentz angle ($\Delta tan(\theta_{LA})$) have been reported using 2017 collision data of CMS. The data is collected in both deconvolution and peak mode. For the measurement of backplane corrections, a variable called Δu has been introduced which is obtained by taking the difference of shifts in the deconvolution mode and the peak mode sensors position. Where the shift itself is defined as the difference between local x and reconstructed local x of track or hits at the sensor position. A straight line fit has been performed to Δu vs $tan(\theta)$ to estimate backplane correction (Δw) and Lorentz angle shift ($\Delta tan(\theta_{LA})$) for tracker outer barrel (TOB). The values of Δw and $\Delta tan(\theta_{LA})$ for six layers of TOB are given in table 5.1. The value of shifts (Δu) in the sensor position and Lorentz angle are measured with the the implementation of cut on track momentum $P_{trk} > 0.8$ GeV. The minimum absolute value of backplane correction (Δw) is 0.39 ± 0.29 μm and the maximum absolute value of backplane correction (Δw) is found to be 2.37 ± 0.66 μm for different layers of TOB. The maximum value of $\Delta tan(\theta_{LA})$ is 0.0000390 ± 0.0000065.

The Backplane corrections Δw and Lorentz angle shifts $\Delta tan(\theta_{LA})$ are also estimated for the miscalibrated geometry setup, where the peak mode data is miscalibrated with corrections derived in deconvolution mode. Results of the fit performed are shown in table 5.3. The minimum absolute value of backplane correction is 0.45 ± 0.29 μm and the maximum absolute value of backplane correction is 2.37 ± 0.66 μm. The maximum value of Lorentz angle shift ($\Delta tan(\theta_{LA})$) is 0.0000380 ± 0.000065. The measure value of backplane corrections correspond to the official limit of the CMS.

Bibliography

[1] A. Einstein. *The Foundation of the General Theory of Relativity.* Annalen Phys: 769–822,1916.

[2] Planck Collaboration, P. Ade et al. *Planck 2013 results. I. Overview of products and scientific results.* arXiv: 1303.5062 [astro-ph.CO].

[3] K. Kodama et al. *Observation of tau-neutrino interactions.* Phys. Lett., B504: 218–224, 2001.

[4] S. L. Glashow, J. Iliopoulos, and L. Maiani *Weak interactions with lepton-hadron symmetry.* Phys. Rev. D, 2(7): 1285.1292, Oct 1970.

[5] V. K. Mittal, R. C. Verma, S. C. Gupta. *Introduction to nuclear and particle physics.* ISBN-978-81-203-4311-5, Apr 2011.

[6] K Nakamura et al. *Review of particle physics.* J. Phys., G37: 075021, 2010.

[7] (ed.) Evans and (ed.) Bryant. *LHC Machine.* JINST, 3: S08001, 2008.

[8] CERN Press Office. *Cern announces lhc to run in 2012.* http://public.web.cern.ch/press/pressreleases/Releases2011/PR01.11E.html, January 2011.

[9] ALICE collaboration. *The ALICE experiment at the CERN LHC.* JINST, 3: S08002, 2008.

[10] LHCb collaboration. *The LHCb Detector at the LHC.* JINST, 3: S08005,

2008.

[11] ATLAS collaboration. *The ATLAS Experiment at the CERN Large Hadron Collider.* JINST, 3: S08003, 2008.

[12] LHCf collaboration. *The LHCf detector at the CERN Large Hadron Collider.* JINST, 3: S08006, 2008.

[13] CERN Accelerating science. *The Large Hadron Collider.* https://home.cern/topics/large-hadron-collider.

[14] CMS collaboration (2008). *The CMS experiment at the CERN LHC.* JINST, 3: S08004, 2008.

[15] G. A. Giurgiu and for the CMS collaboration. *Pixel Hit Reconstruction with the CMS Detector.* ArXiv e-prints, August 2008.

[16] V. Radicci. *Operational experience and performance of the cms pixel detector during the first LHC beams. Technical Report CMS-CR-2010-117.* CERN-CMSCR-2010-117, CERN, Geneva, Jul 2010.

[17] S. Gadomski, G. Hall, T. S. Høgh, P. Jalocha, E. Nygard, and P. Weilhammer. *The deconvolution method of fast pulse shaping at Cadron Colliders.* 1992.

[18] V. Khachatryan, A. M. Sirunyan, A. Tumasyan, W. Adam, T. Bergauer, M. Dragicevic, J. Ero, C. Fabjan, M. Friedl, R. Fruhwirth, and et al. *CMS tracking performance results from early LHC operation.* European Physical Journal C, 70:1165–1192, December 2010.

[19] W. -M. Yaoetal. *Review of Particle Physics.* Journal of G,33: 258–270, 2006.

[20] D. Landau. *On the Energy Loss of Fast Particles by Ionization.* In Collected Papers of L. D. Landau. Pergamon Press, Oxford, 1965.

[21] H. Bichsel. *Straggling in thin silicon detectors.* Reviews of Modern Physics, 60(3): 664–669, 1988.

[22] S. Ramo. *Currents Induced by Electron Motion.* Proceedings of the I.R.E. 27, 27: 584– 585, 1939.

[23] CMS collaboration. *CMS silicon strip.* http://cms.web.cern.ch/news/silicon-strips.

[24] M. Raymonda, G. Cervellib, M. Frenchc, J. Fulchera, G. Halla, L.Jonesc, L-K. Lima, G. Marseguerrad, P. Moreirab, Q. Morrisseyc, A. Nevianic,d, E. Noaha . *The CMS Tracker APV25 0.25 μm CMOS Readout Chip.*.

[25] L. L. Jones, M. J. French, Q. Morrissey, A. Neviani, M. Raymond, G. Hall, P. Moreira and G. Cervelli. *The APV25 deep submicron readout chip for CMS detectors.* Conf. Proc. C **9909201**, 162 (1999).

[26] P. Lenzi, C. Genta, and B. Mangano. *Track reconstruction of real cosmic muon events with CMS tracker detector.* J. Phys. Conf. Ser. 119 (2008) 032030.

[27] R. Fruhwirth. *Application of Kalman filtering to track and vertex fitting.* Nucl. Instrum. Meth. A262 (1987) 444–450.

[28] M. J. French et al. *Design and results from the APV25, a deep submicron CMOS front-end chip for the CMS tracker.* Nucl. Instrum. Meth. A 466 (2001) 359.

[29] M. Raymond et al. *Final result from the APV25 production wafer testing.* in Proceedings of the 11th Workshop on Electronics for LHC and Future Experiments (Heidelberg), p. 91. 2005.

[30] Andrea Venturi. *The CMS Collaboration. CMS Back Plane Corrections.* https://twiki.cern.ch/twiki/bin/viewauth/CMS/BackPlaneCorrections.